RSC Advances

PAPER

View Article Online
View Journal | View Issue

Cite this: *RSC Adv.*, 2025, **15**, 48566

Isolation and characterization of bioactive constituents from *Withania coagulans* Dunal with antioxidant and multifunctional enzyme inhibition potential, supported by docking, MD, and DFT studies

Hayat Bibi,[a] Saima Maher,*[a] Noureen Khan,[b] Shamim Khan,[c] Tahir Ali Chohan,[d] Hammad Saleem,[b] Magda H. Abdellattif,[e] Ajmal Khan*[fg] and Ahmed Al-Harrasi*[f]

Withania coagulans Dunal is a medicinal plant with potential therapeutic applications in neurodegenerative and metabolic disorders. This study aimed to isolate, structurally characterize, and evaluate the biological potential of withanolide-type compounds from *Withania coagulans* Dunal, with a focus on their antioxidant and enzyme inhibitory activities relevant to neurodegenerative and metabolic disorders. Two new withanolides (**WTH1** and **WTH2**) and one known compound (**WTH3**) were isolated from *W. coagulans*. The methanol extract and its fractions were assessed for total phenolic and flavonoid contents, antioxidant capacity (DPPH, FRAP, phosphomolybdenum assays), and enzyme inhibitory activities against acetylcholinesterase (AChE), butyrylcholinesterase (BChE), lipoxygenase, α-glucosidase, and tyrosinase. The methanol extract exhibited the highest total phenolic (71.53 mg GAE per g) and flavonoid (64.32 mg QE per g) contents, correlating with strong antioxidant activity (DPPH: 91.2%, FRAP: 678.3 μmol Fe^{2+} per g, phosphomolybdenum: 4.2 mmol TE per g). It showed significant inhibitory effects against AChE (4.10 mg GALAE per g), BChE (3.71 mg GALAE per g), lipoxygenase, α-glucosidase, and tyrosinase, with the ethyl acetate fraction displaying the strongest α-glucosidase inhibition (3.51 mmol ACAE per g). *In silico* docking revealed strong binding affinities of **WTH1** and **WTH3** toward AChE (−11.616 and −11.438 kcal mol^{-1}, respectively), while **WTH3** also interacted effectively with BChE (−9.30 kcal mol^{-1}), surpassing the standard drug physostigmine (−5.85 kcal mol^{-1}). Pharmacokinetic evaluation of **WTH1** predicted high gastrointestinal absorption (97.65%), moderate oral bioavailability (0.55), and absence of hepatotoxicity or AMES toxicity. DFT analysis indicated a stable HOMO–LUMO energy gap (9.923 eV), and binding free energy calculations confirmed strong interaction of **WTH1** with AChE using PB (−29.731 kcal mol^{-1}) and GB (−43.54 kcal mol^{-1}) methods, outperforming the reference drug (−15.08 kcal mol^{-1}). The findings demonstrate that *W. coagulans* methanol extract, particularly the isolated new withanolide **WTH1**, exhibits potent antioxidant and enzyme inhibitory activities with promising pharmacokinetic properties. These results support further pharmacological and clinical evaluation of *W. coagulans* as a natural source of therapeutic agents against neurodegenerative and metabolic disorders.

Received 25th June 2025
Accepted 26th November 2025

DOI: 10.1039/d5ra04491j

rsc.li/rsc-advances

1. Introduction

Natural products have long played a pivotal role in the discovery of bioactive molecules and therapeutic agents due to their remarkable chemical diversity and pharmacological potential. More than 80% of the world's population relies on traditional plant-based medicines for primary healthcare needs, and their global market value continues to grow substantially.[1,2] In many countries, traditional therapies account for 30–60% of total medicinal use, and in developed nations like Germany, up to

[a]*Department of Chemistry, Sardar Bahadur Khan Women University, Quetta, Pakistan. E-mail: saimamaher@yahoo.com*

[b]*Department of Chemistry, Rawalpindi Women University, 6th Road, Satellite Town, Rawalpindi 46300, Pakistan*

[c]*Department of Chemistry, Sardar Bahadur Khan Women University, Quetta, Pakistan*

[d]*Institute of Pharmaceutical Sciences (IPS), University of Veterinary & Animal Sciences (UVAS), Lahore, Pakistan*

[e]*Chemistry Department, College of Sciences, University College of Taraba, Taif University, P.O. Box 11099, Taif 21944, Saudi Arabia*

[f]*Natural and Medical Sciences Research Center, University of Nizwa, PO Box 33, 616 Birkat Al Mauz, Nizwa, Oman. E-mail: ajmalkhan@unizwa.edu.om; aharrasi@unizwa.edu.om*

[g]*Department of Chemical and Biological Engineering, College of Engineering, Korea University, Seoul 02841, Republic of Korea*

90% of the population has reported using natural products for various health issues.[2] The increasing global demand for herbal medicines has led to an estimated annual revenue of nearly $60 billion, which continues to grow.[3] Among the medicinal plants of traditional importance, the genus *Withania* (family: Solanaceae) holds notable therapeutic and economic value. This genus comprises about 23 species distributed across South Asia, North Africa, the Mediterranean, Southern Europe, and Western Asia.[4,5] In Pakistan, two species *Withania somnifera* (ashwagandha) and *Withania coagulans* (Ashutosh booti) are of particular significance due to their long-standing use in traditional medicine.[6,7] *W. coagulans* is especially recognized for its pharmacological properties, including its application in treating conditions such as insomnia, impotence, stunted growth in children, and degenerative diseases.[8] Its fruits possess sedative, emetic, and diuretic effects, while its seeds are used for milk coagulation, attributed to their active phytochemical constituents.[9] The berries of *W. coagulans* primarily contain fatty oils, free amino acids, and withanolides.[10] Various species of the *Withania* genus have long been used in traditional medicine for the treatment of a wide range of ailments, including fevers and skin disorders.[11] Among them, *W. coagulans* is particularly noted for its diverse therapeutic applications. Traditionally, it has been used to manage conditions such as impotence, chronic diseases, stunted growth in children, insomnia, and nervous exhaustion. Its fruits, which are slightly sweet in taste, are believed to possess sedative, emetic, and diuretic properties.[12] Despite the growing interest in these traditional uses, comprehensive scientific evaluations of its pharmacological potential remain limited. Moreover, the mechanisms underlying its therapeutic effects are not yet fully understood.[12]

Different parts of the plant have also been employed in folk medicine for the treatment of rheumatism, dropsy, ulcers, and age-related debility.[13] The wild fruits of *W. coagulans* exhibit various nutraceutical and biological activities, making them potentially valuable for promoting health and wellness.[14–16] Much of the plant's medicinal value is attributed to its characteristic withanolides a class of steroidal lactones chemically defined by the presence of a γ- or δ-lactone side chain at the C-17 position.[17,18] Withanolides have also been identified in other families such as Taccaceae, Leguminosae, and Solanaceae, as well as from marine organisms.[19]

Previous reports have highlighted the broad pharmacological potential of *W. coagulans*, including antioxidant, antidiabetic, anti-inflammatory, and neuroprotective effects. However, despite these promising activities, systematic isolation and structural characterization of its active constituents, and their mechanistic evaluation against key biological targets, remain limited. A deeper understanding of its bioactive compounds and their molecular interactions is essential to substantiate its traditional uses and explore its therapeutic potential.

In addition, *W. coagulans* has shown promising antidiabetic and antiglycation properties, with several bioactive compounds identified as contributors to its antidiabetic activity.[23,24] Further studies have demonstrated its antimutagenic, leishmanicidal, and additional antidiabetic effects.[21,25,26] Notably, two unique withanolides chantriolides D and E were isolated from *Tacca chantrieri* and shown to exert selective cytotoxic effects against cancer cell lines.[27]

Therefore, the present study was designed to isolate and structurally characterize bioactive withanolide compounds from *W. coagulans* and to evaluate their antioxidant and enzyme inhibitory properties using *in vitro* and *in silico* approaches. The investigation particularly focused on enzymes linked to major chronic conditions, including acetylcholinesterase and butyrylcholinesterase (neurodegeneration), α-glucosidase (diabetes), lipoxygenase (inflammation), and tyrosinase (skin disorders). By integrating phytochemical analysis, biological assays, molecular docking, and computational modeling, this study aims to elucidate the pharmacological relevance of *W. coagulans* and identify potential lead compounds for future drug discovery efforts. The present study aimed to evaluate the enzyme inhibitory activities of whole-plant extracts prepared using solvents of varying polarity. These extracts were assessed for their inhibitory effects against key enzymes linked to major health disorders: acetylcholinesterase and butyrylcholinesterase (neurodegenerative diseases), α-glucosidase (diabetes), lipoxygenase (inflammation), and tyrosinase (hyperpigmentation). Furthermore, the antioxidant potential of the extracts was determined using three standard assays: phosphomolybdenum, DPPH radical scavenging, and ferric reducing antioxidant power (FRAP). In addition, total bioactive contents were quantified *via* spectrophotometric assays, and major constituents were isolated using chromatographic techniques. Future investigations should focus on the isolation and structural characterization of bioactive compounds from *Withania coagulans*, particularly withanolides, to better understand their pharmacological mechanisms. *In vivo* studies are essential to validate its enzyme inhibitory and antioxidant potential. Toxicological assessments will help establish safety for therapeutic use. Formulation of standardized extracts could lead to the development of herbal drugs. Omics-based approaches may reveal biosynthetic pathways for key metabolites. Overall, this plant holds strong potential for future drug discovery and nutraceutical applications.

Despite the extensive traditional uses of *W. coagulans*, there remains a lack of detailed studies linking its phytochemical constituents to specific biological activities. Therefore, the present study was designed to isolate and structurally characterize bioactive compounds from *W. coagulans* and to evaluate their antioxidant and enzyme inhibitory properties, targeting key enzymes associated with neurodegenerative, metabolic, and inflammatory disorders. This integrated approach combining phytochemical characterization, bioassays, and computational modeling aims to elucidate the molecular mechanisms underlying the plant's pharmacological potential and to identify promising natural lead compounds for therapeutic development.

2. Material and methods

2.1. Plant collection and extraction

The plant *W. coagulans* (Stocks) Dunal was collected from the sub urban zones of Karachi, Pakistan, the plant was Taxonomically identified by Dr Sher Wali Khan, taxonomist a voucher specimen

(No. 46257) was deposited in the Herbarium of Botany Department, University of Karachi, Karachi-75270, Pakistan. The dried plant material (1 kg) was soaked 100% in methanol (3 × 3 L). The crude extract was filtered and evaporated at room temperature. The yields of the resulting solvent fractions were: *n*-hexane 12.5 g (12.5%), chloroform 20.0 g (20%), ethyl acetate 17.0 g (17%), *n*-butanol 30.0 g (30%), and aqueous 20.5 g (20.5%). Each solvent mixed with methanol extract solution equally in a separate funnel by shaking for 3 min. Rotary evaporation was used at 40 °C for organic solvent layers concentrate to dryness, and the water-soluble fraction freeze-dried.

2.1.1. Phytochemical composition and antioxidant

2.1.1.1. Total phenolic (TPC) and flavonoid content (TFC). The total phenolic content (TPC), a volume of 0.25 mL from the sample stock solution (1 mg mL^{-1}) was combined with 1 mL of Folin–Ciocalteu reagent, previously diluted at a ratio 1 : 9, v/v. Subsequently, 0.75 mL of 1% Na_2CO_3 solution was added to a mixture after allowing the reaction mixture for 3 minutes, it was incubated for two hours and then the sample absorbance was observed at 760 nm. For the estimation of total flavonoid content, 1 mL of the sample solution (1 mg mL^{-1}) was combined with 1 mL of 2% aluminium chloride solution prepared in methanol, the mixture was incubated at room temperature for 10 minutes, and then the absorbance was recorded at 415 nm The results of total phenolic constituents were reported as equivalents of gallic acid (mg GAE per g extract), however the results of total flavonoid constituents were recorded as equivalents of quercetin (mg QE per g extract).[1,2]

2.1.2. Isolation and chemical characterization of pure compounds from *Withania coagulans*

2.1.2.1. Extraction and fractionation. The dried plant material (1 kg) was soaked in 80% methanol–water (3 × 3 L). The extract was filtered and evaporated at room temperature. The methanolic extract (100 g) was re-suspended successively partitioned with *n*-hexane, $CHCl_3$, EtOAc, and *n*-butanol. Each solvent mixed with methanol extract solution equally in a separate funnel by shaking for 3 min. Rotary evaporation was used at 40 °C for organic solvent layers concentrate to dryness, and the water-soluble fraction freeze-dried.

2.1.2.2. Purification of pure compounds. The MeOH fraction (*ca.* 200 g) of the plant *W. coagulans* (Stocks) Dunal was partitioned with *n*-hexane, $CHCl_3$, *n*-butanol and water as shown in Fig. 1. The $CHCl_3$ fractions were made on pH = 3, 7 and 10. The fraction (pH-3) (19 g) was subjected on flash silica column chromatography with $CHCl_3$/*n*-hexane and three sub fractions (CCW = 1) eluted with at 100% *n*-hexane, 50% $CHCl_3$/*n*-hexane and 75% $CHCl_3$/*n*-hexane. Fraction (MC = 2) 50% $CHCl_3$/*n*-hexane (7.3 g) reloaded on silica gel column chromatography and then eluted different sub fractions (Fr. 1–7). Fraction 1 (3.3 g) was subjected to column chromatography and this led to the isolation of known compounds withanolides G, coagulin G and stigmasterol.

*2.1.2.3. Isolation of new compounds (**WTH1** and **WTH2**).* The $CHCl_3$ fraction 4 was further subjected to polyamide column chromatography, and eluted with acetone/chloroform by polarity base. Four sub fractions were resulted by polyamide column chromatography. The eluted fraction 4A (20% acetone/$CHCl_3$) (4.8 gm) was loaded to a silica gel column, and five main fractions (Fr = WC-pH-A-E) were recovered. Fraction WC-pH-B (25 mg) was further fractionated on normal phase recycling HPLC (20% isopropylalcohol/*n*-hexane) for semi purification and then obtained five fractions. Then repeated separately pencil column chromatography on silica gel, with 8% $CHCl_3$/*n*-hexane and resulted compounds new chemical components as

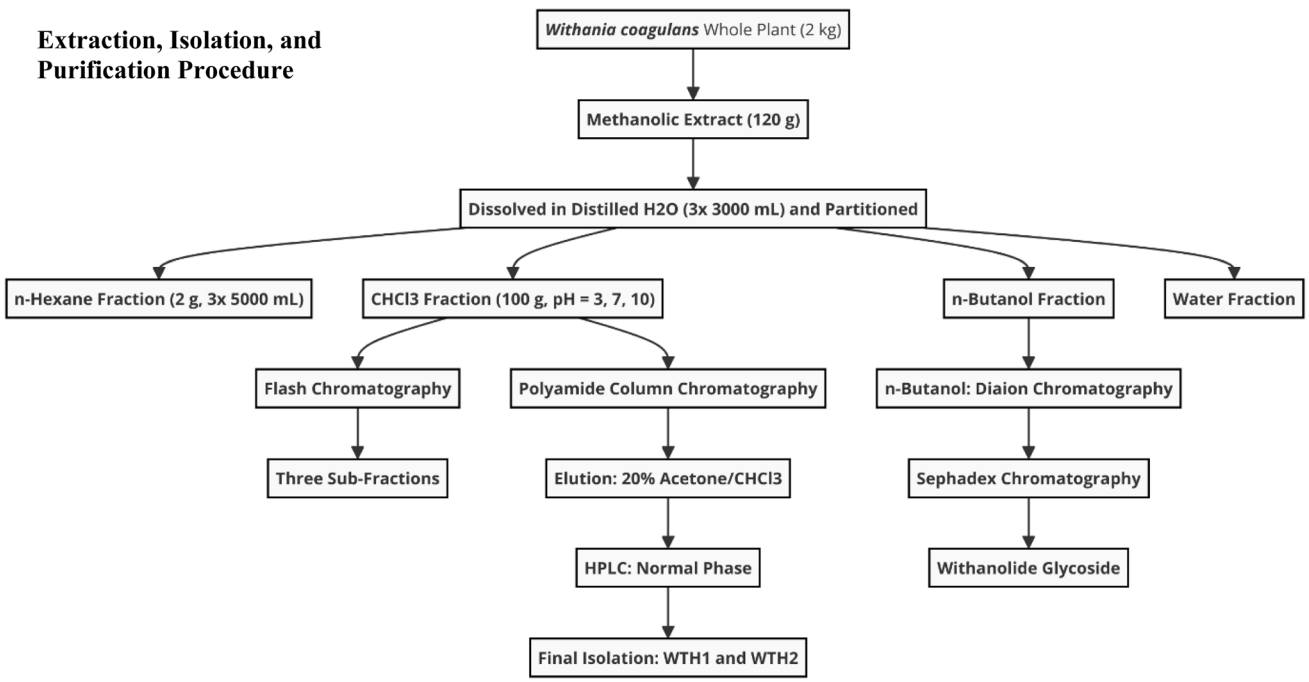

Fig. 1 The flowchart depicts the stepwise process for extracting and purifying bioactive compounds from *Withania coagulans*, highlighting partitioning, chromatographic techniques, and final compound isolation (WTH1 and WTH2).

compounds-**1** (**WTH1**), and compounds-**2** (**WTH2**) was obtained (Fig. 7).

*2.1.2.4. Isolation of known compound (**WTH3**).* The *n*-butanol fraction (35 g) was subjected to column chromatography on Diaion HP-20 and eluted with water, water–methanol, methanol in decreasing order of polarity to collect five fractions. The fraction obtained with H_2O : MeOH (1 : 1, 8.5 g), was rechromatographed on sephadex LH-20 and elution was carried out with various mixtures of H_2O–MeOH in decreasing order of polarity. The sub-fractions obtained with H_2O–MeOH (6 : 4) (1.2 g), was re-chromatographed over polyamide resin eluting with CH_2Cl_2 : MeOH to afford the semi-pure fractions, which were further purified by re-chromatographed over silica gel and eluted with $CHCl_3$: MeOH (8.5 : 1.5) and $CHCl_3$: MeOH (8.2 : 1.8) to afford known withnolideglycoside (**WTH3**) (Fig. 7).

2.1.2.5. Spectroscopic characterization. Shimadzu UV 240 machine was used for recording UV Spectra in methanol at λ_{max} (log ε). IR spectra was taken on JASCO. ^{1}H and ^{13}C-NMR spectra were noted on Bruker AV-500 spectrometer operating at 300, 500 MHz, respectively, and the data is given in δ (ppm). Bruker AMX 500 NMR spectrometer was used for 1 and 2D nuclear magnetic resonance (NMR) spectroscopy. Molecular form was confirmed through EI-MS at 70 eV on a Finnigan MAT-112 or MAT-312 presented as *m*/*z* (%). Glycerol matrix was used for FAB-MS on a JEOL HX-110 mass spectrometer. Recycling HPLC with columns ODS H-80 or L-80 (JAI, LC-908W, Japan Analytical Industry Co. Ltd) was used for final purification of compounds. The isolated compounds (**WTH1**–**WTH3**) were characterized by UV, IR, ^{1}H and ^{13}C NMR, 2D NMR (COSY, HSQC, HMBC, NOESY), and mass spectrometry (EI-MS, FAB-MS, HR-EIMS). Spectral data were compared with literature values to confirm structural assignments. Complete NMR and MS data are provided in the SI (Fig. S1–S8).

2.2. Biological activities

2.2.1. Antioxidant assays. All antioxidant assays (DPPH, FRAP, and phosphomolybdenum) were performed by the authors following the protocols described by Grochowski *et al.* (2017) with minor modifications. Calibration curves were prepared using Trolox as a standard (10–200 μg mL^{-1}, R^2 = 0.998), and the antioxidant capacities were expressed as milligrams of Trolox equivalents per gram of extract (mg TE per g). Total phenolic and flavonoid contents were quantified using gallic acid (10–100 μg mL^{-1}, R^2 = 0.997) and quercetin (10–100 μg mL^{-1}, R^2 = 0.996) calibration curves, respectively, and expressed as mg GAE per g and mg QE per g of extract. CUPRAC and metal-chelation assays were not included in the present study; instead, the combination of DPPH, FRAP, and phosphomolybdenum methods was used to provide a comprehensive evaluation of radical-scavenging and reducing activities.[2]

2.2.2. Free radical scavenging activity (DPPH). 1 mL of the extract was added to 4 mL, DPPH solution (0.267 mM in 0.004% methanol), and the reaction mixture was kept at room temperature in dark for 30 minutes and then the absorbance was recorded at 517 nm. Milligrams of Trolox equivalents per gram of dry extract (TE per g extract) were the measure unit.

2.2.2.1. Phosphomolybdenum method. To evaluate total antioxidant capacity 0.3 mL of the sample solution was mixed with 3 mL of reagent solution the composed solution of 0.6 M sulfuric acid, 28 mM sodium phosphate and 4 mM ammonium molybdate and incubated at room temperature for 90 minutes. The absorbance was measured at 695 nm. The antioxidant activity was quantified in term of millimoles of Trolox equivalents per gram of dry extract (mmol TE per g extract).

2.2.2.2. Ferric reducing antioxidant power (FRAP) method. 0.1 mL of the sample solution was added to reagent (2 mL) in acetate buffer (0.3 M, pH 3.6), 2,4,6-tris(2-pyridyl)-s-triazine (TPTZ) (10 mM) in 40 mM HCl and ferric chloride (20 mM) in a final ratio of 10 : 1 : 1 (v/v/v) and the absorbance was recorded at 593 nm 30 min. Milligrams of Trolox equivalents per gram of dry extract (TE per g extract) were the measurement unit.

2.2.2.3. Enzyme inhibition assays. The enzyme inhibitory capability of all extracts were examined against acetylcholinesterase (AChE), butyrylcholinesterase (BChE), tyrosinase, and α-amylase using established *in vitro* bioassays protocol it were described in previous studies.[2]

2.2.2.4. Cholinesterase. The reaction mixture contained of 50 μL of the sample, 125 μL of DTNB (3 mM), and 25 μL of enzyme solution (0.265 U mL^{-1} for AChE or 0.026 U mL^{-1} for BChE) in Tris–HCl buffer (pH 8.0). Subsequently, 25 μL of substrate either acetylthiocholine iodide (15 mM) or butyrylthiocholine chloride (1.5 mM) was added. And then incubation at room temperature for 15 minutes The absorbance was recorded at 405 nm. Enzyme inhibition was stated as milligrams of galantamine equivalents per gram of dry extract (mg GALAE per g).

2.2.2.5. α-Amylase. The α-amylase inhibition assay was performed following the method of Grochowski *et al.* (2017) with slight modifications.[2] Calibration was carried out using acarbose as the standard (10–100 μg mL^{-1}, R^2 = 0.995). Inhibition (%) was calculated as

$$\text{Inhibition (\%)} = [(A\_\text{control} - A\_\text{sample})/A\_\text{control}] \times 100$$

and results were expressed as mmol acarbose equivalents (ACAE) per g of extract.

The reaction mixture composed by 25 μL of the sample solution and 50 μL of the α-amylase solution (10 U mL^{-1}) in phosphate buffer (pH 6.9 with 6 mM sodium chloride) was added to 50 μL of the starch solution (0.05%) and the reaction was stopped with the addition of 25 μL of HCl (1 M). Then 100 μL of the iodine-potassium iodide solution was added. After 10 min of incubation, the absorbance was recorded at 630 nm and the results expressed as millimoles of acarbose equivalents per gram of dry extract (ACAEs per g extract).

2.2.2.6. Tyrosinase. 25 μL of the sample solution were added to a 40 μL of tyrosinase solution (200 U mL^{-1}) and phosphate buffer (40 mM, 100 μL, pH 6.8) in a 96-well microplate and incubated for 15 min at 25 °C. Then the reaction was initiated by adding l-DOPA (10 mM, 40 μL). After 10 min of incubation at room temperature, the absorbance was recorded at 492 nm and the results expressed as milligrams of kojic acid equivalents per gram of dry extract (KAE per g extract).

2.3. Computational methods

2.3.1. Structure preparation and molecular docking studies. Molecular docking, a key computational method in structural biology and drug discovery, predicts interactions between ligands and target proteins, revealing atomic-level details like hydrogen bonds and hydrophobic interactions.[3–5] At first, acetylcholinesterase (AChE), butyrylcholinesterase (BChE), tyrosinase (TYR), and lipoxygenase (LOX) co-crystallized structures were downloaded from the RCSB Protein Data Bank with the following PDB entries: 4EY7[6], 6QAE,[7] 5M8N,[8] and 3O8Y[9] respectively. However, the co-crystal structure of *Saccharomyces cerevisiae* alpha-glucosidase (GLU) is not yet known. We have used the glucosidase protein's previously established and well confirmed 3D-conformation in this paper, as shown in our earlier work.[10,11] Before docking, protein structures were meticulously prepared using Maestro Protein Preparation Wizard, which involved cleaning, adding missing hydrogens and heteroatoms, optimizing side chain orientations, and confirming amino acid protonation states.[12,13] To identify the best isolated compound responsible for the enzyme inhibitory potential of *W. coagulans*, molecular docking investigations were undertaken. Initially, 2D structures of the phytoconstituents **WTH1**, **WTH2**, and **WTH3**, isolated from the DCM extract of *W. coagulans* and detected *via* GCMS, were generated using ChemDraw 16.0. The 2D structures of all compounds (polar and non-polar hydrogens) were converted to 3D bioactive conformations after protonation, and the energy was then reduced up to a gradient of 0.01.[14] LigPrep in Maestro generated stable tautomeric, stereochemical, and ionization variants, and OPLS4 force field optimized ligands to their lowest energy conformations.[15] The receptor grid was built using the prepared protein. These grids were created using the OPLS 2005 force field.[16] The protein atom van der Waals radii were adjusted with a scaling factor of 1.0, and a charge cutoff of 0.25 determined polarity. Receptor grid box dimensions of 20 Å in each direction were centered around the ligands, ensuring ample space in the binding pocket for ligand accommodation.[17] A cubic docking grid, centered on binding site of each protein and designed to fit ligands up to ≤20 Å, was established. We utilized Glide's extra precision (XP) scoring, permitting full ligand flexibility.[18] The Maestro attempted to fit the ligands into the binding site, exploring various orientations and conformations. Each ligand pose was assessed and scored for predicted stability and binding affinity in the protein active site. Post-docking, results were analyzed to pinpoint inhibitors with the greatest potential, considering docking scores and interaction profiles.[19,20]

2.3.2. Toxicological modelling and ADME profiling. ADME profiling is integral to discerning the pharmacokinetic attributes of pharmaceutical agents, thereby facilitating crucial decision-making processes, dosage formulation, and enhancing the efficacy of drug development programs. By elucidating the absorption, distribution, metabolism, and excretion characteristics of drug candidates, ADME profiling serves as an expedient tool in the intricate sphere of pharmaceutical development. This avant-garde technique enables researchers to quickly pinpoint potential obstacles and constraints, strategically steering the optimization process to optimize resource allocation and accelerate the journey toward the creation of safe and efficacious medicinal compounds. Swiss-ADME web tool (http://www.swissadme.ch) was used to evaluate synthetic merchandising potential of these compounds. The pkCSM web application (https://biosig.lab.uq.edu.au/pkcsm/prediction) together with its theoretical background at (https://biosig.lab.uq.edu.au/pkcsm/theory) was employed to forecast the *in silico* ADMET properties of compounds **WTH1**, **WTH2** and **WTH3**. The Swiss ADME and pkCSM platforms offer swift access to data analysis and an in-house compound library, simplifying the identification of optimal candidates for future development based on their ADME characteristics.

2.3.3. DFT studies/MESP/HOMO/LUMO analysis. Density functional theory (DFT) calculations were performed with slight modifications in accordance with the methods described in ref. 21. The B3LYP functional and SVP basis set were employed throughout the calculations, affirming their effectiveness in determining the electronic structures of atoms and molecules. The research examines multiple essential parameters which involve optimized geometric properties together with frontier molecular orbital (FMO) energy values along with both overall and specific reactivity indexes as well as molecular electrostatic potential (MEP). The essential factors help to understand chemical behavior and reactivity of investigated molecules which enables valuable insights for theoretical and practical usage. The checkpoint files generated from simulations were examined under Gauss View 6 for extensive evaluation of electronic density distribution and potential energy surface analysis.

2.3.4. Molecular dynamics simulations. The docking simulations analyzed potent and moderate AChE inhibitors structurally but MD simulations later stabilized these structures by placing them in solution conditions. The simulations executed using AMBER20 with ff99SB force field implemented in the package.[22] The docking models comprising virtual screening-derived compounds attached to AChE received MD simulations to assess their dynamic stability together with binding interactions when displayed as Fig. 4(A–G). The MM/PB(GB)SA method got implemented to assess binding affinities between the AChE-eserine and AChE-**WTH1** complexes specifically.[23] All MD simulations, along with molecular mechanics-based free energy calculations (MM/PB(GB)SA), were carried out within the AMBER16 software framework.[24] The AMBER16 software framework ran both MD simulations as well as MM/PB(GB)SA free energy calculations following established parameters.[5,11,25] The supplementary materials contain full descriptions about the accepted methodologies utilized in this research work.

2.4. Statistical analysis

The assays were carried out in a triplet, and independent experiments and the results were calculated as a mean value ± standard deviation (SD). SPSS v.17.0 software was used for data analysis. One-way analysis of variance *via* ANOVA followed by Tukey's test was done to find out the differences between means. The significant statistical value of $p < 0.05$ was obtained.

3. Results and discussion

3.1. Phytochemical composition and antioxidant properties

In a comparative analysis of bioactive contents and antioxidant activities from different extracts of *W. coagulans*, significant variations in the efficacy of solvent extraction were observed, as evidenced by the quantification of TPC, TFC, and antioxidant activities measured *via* DPPH, FRAP, and phosphomolybdenum assays (Table 1). The methanol extract demonstrated the highest TPC at 71.53 mg GAE per g and also excelled in DPPH radical scavenging activity with a value of 113.45 mg TE per g extract. These results suggest that methanol is particularly effective in extracting phenolic compounds, which are well-known for their potent antioxidant properties. Similarly, this extract also showed high FRAP activity at 173.53 mg TE per g extract, further corroborating its superior capability in yielding bioactive compounds with strong electron donation capabilities. Conversely, the *n*-hexane extract, while displaying the lowest phenolic (12.74 mg GAE per g) and flavonoid (9.31 mg QE per g) contents among the tested solvents, exhibited a surprisingly high phosphomolybdenum value of 73.69 mg TE per g extract. This indicates that *n*-hexane may preferentially extract other classes of antioxidants, which do not conform to the typical phenolic or flavonoid structures but demonstrate considerable antioxidant capacity. The chloroform extract yielded moderate levels of TPC and TFC (33.91 mg GAE per g and 45.71 mg QE per g, respectively) and showed good antioxidant activity in the DPPH assay (93.24 mg TE per g extract), suggesting a balanced profile in extracting flavonoids and other phenolic antioxidants. The EA extract followed a similar pattern, with TPC and TFC values at 54.8 mg GAE per g and 39.87 mg QE per g, respectively, accompanied by robust antioxidant activities. The *n*-butanol extract presented a unique profile with a relatively high phenolic content at 62.94 mg GAE per g and moderate antioxidant activities across all assays. Although it did not lead in any specific category, its performance across different measures suggests a generalized capability in extracting a variety of antioxidant compounds.

The data, reflecting means from three repetitions with standard deviations, was statistically analyzed, and significant differences ($p < 0.05$) were noted among the extracts, indicating that the choice of solvent critically influences the extraction efficiency and the type of bioactive compounds obtained. These findings emphasize the necessity for selecting appropriate extraction solvents based on the desired chemical profile for applications in nutraceuticals and pharmaceutical formulations. Future studies should focus on identifying the specific antioxidant compounds extracted by *n*-hexane and exploring the biological implications of the extracts' antioxidant capacities in *in vivo* systems.

3.2. Isolation of pure compounds

The **WTH1** was found to be a 2,4,6-triene 1-one and its structure developed on the basis of spectral data. It was obtained as colorless powder. The UV spectrum MeOH of ($C_{28}H_{36}O_5$) indicated absorption at 352 and 228 nm are good evidence for such a system in ring A and B and for unsaturated δ lactone system of the side chain. The HR-EIMS of **WTH1** afforded an M^+ peak at *m*/*z* 452.2654 corresponding to the molecular formula $C_{28}H_{36}O_4$ The IR spectrum showed band at 3426, 1712 and 1684 cm^{-1} presence of hydroxyl, six membered cyclic keton and α, β unsaturated lactone moiety. The ^1H and ^{13}C-NMR data specified positive for three tertiary methyl and one secondary methyl, six methylene (one oxygen containing methylene), 10 methine and 8 quaternary carbons (eight olefin carbon and two carbonyl carbon), their ^1H and ^{13}C-NMR shift were assigned based on a combination of 2D NMR [H–H] shift correlation spectroscopy (COSY) and ^1H detected multiple quantum coherence [HMQC] techniques. On a basis of withanolide skeleton 1-conjugated keton, 2,4,6 unsaturated, 20 substituted and 27-hydroxy α,β unsaturated δ-lactone side chain were assigned. It differed from other withanolides. However, the presence of the C-21 methyl as a single indicated that neighboring C-20 had no proton. The low field (δ 1.48) shifts of C-21 methyl. (δ 20.4) indicated that an oxygen functionality may be substituted on C-20. (δ 76.2). The downfield chemical shift of the C-27 as doublet at 4.37 and 4.72 were assigned to two protons of a methylene at C-27. The other methyl singlet was appeared at (δ 1.98) on C-28. The δ 5.83 (dd $J_{2,3} = 9.6$ Hz, $J_{2,4} = 3.2$ Hz), 6.89 (m), 5.28 (br, S), 5.72 (d, $J_{4,3} = 17.7$ Hz) and 6.09 (d, $J = 9$ Hz) represented five olifenic proton at H-2, H-3, H-4, H-6, and H-7, respectively. A downfield methane double doublet at δ 4.37 (dd $J_{22,23\alpha} = 13.2$ Hz, $J_{22,22\beta} = 3.4$ Hz) was agreement to C-22 methine proton of the lactone ring (Table 7).

In the COSY 45°spectrum of **WTH1**, the C-2 methine proton coupling with C-3 methine, and C-6 methine proton with C-7 methine. C-22 methine proton showed vicinal coupling with

Table 1 Total bioactive contents in tested extract/fractions of *Withania coagulans*[a]

	Total bioactive contents		Antioxidant activities		
Extracts	Total phenolic content (mg GAE per g)	Total flavonoid content (mg QE per g)	DPPH (mg TE per g extract)	FRAP (mg TE per g extract)	Phosphomolybdenum (mg TE per g extract)
Methanol	71.53 ± 1.34	64.32 ± 0.52	113.45 ± 1.92	173.53 ± 0.91	32.83 ± 0.39
n-Hexane	12.74 ± 0.92	9.31 ± 1.12	13.54 ± 1.31	24.61 ± 0.92	73.69 ± 1.31
Chloroform	33.91 ± 1.02	45.71 ± 0.21	93.24 ± 0.87	81.04 ± 0.91	51.19 ± 1.31
EA	54.82 ± 1.37	39.87 ± 1.49	106.74 ± 1.52	95.49 ± 1.17	43.92 ± 0.83
n-Butanol	62.94 ± 0.43	49.87 ± 0.32	83.21 ± 0.96	89.42 ± 1.48	23.41 ± 0.93

[a] Data from three repetitions, with mean ± standard deviation; means with different superscript letters in the same column are significantly ($p < 0.05$) different. GAE: gallic acid equivalent; QE: quercetin equivalent.

the C-23 methylene proton. The ^{13}C-NMR spectra showed the signal δ 128.2, 148.1, 119.6, 127.7 and 130.2 were assigned to vinylic carbon (C-2, C-3, C-4, C-6, and C-7, respectively). In ring A and B. while the peak at δ 149.0, 136.1 and 122.8 were attributed to the quaternary vinylic carbon (C-24, C-5 and C-25, respectively). The oxygen bearing methane carbon were at δ 83.5 (C-22) and at δ 58.5 for C-27 methylene carbon. The signal appearing at δ 20.2, 25.5, 18.5, and 12.5 were assigned to the C-28, C-21, C-19, C-18 methyle, respectively in Table 1. In the HMBC spectrum of **WTH1**, (C-19) methyl proton (δ 1.31) showed correlation with carbon resonating at δ 58.5 (C-10), δ 203.1 (C-1), and δ 148.1 (C-3), the C-3 proton (δ 6.89) indicated correlations with the down field carbon resonating at δ 203.1 (C-1) and 136.1 (C-5). The C-28 methyl proton (δ 1.98) exhibited coupling with C-24 methyl proton showed also interaction with the lactone carbonyl (C-26) resonating at δ 168.2. Whereas, C-28 methyl protons exhibited interaction with C-23 (δ 33.1) (Fig. 8). The stereo chemistry at C-22 was assigned on biogenetic ground and by chemical shift comparison of known withanolide data,[21] the spectroscopy evidences led to structure of **WTH1**. The comprehensive structural and spectroscopic characterization of compound **WTH1**, including ^{1}H and ^{13}C NMR, DEPT experiments, 2D NMR (HSQC, HMBC, COSY, NOESY) for proton-carbon correlations and spatial interactions, as well as GC-MS analysis highlighting the molecular ion peak and fragmentation patterns, is provided in the SI (Fig. S1–S4).

The **WTH2** new compound was isolated from chloroform extract as colourless powder. The electron impact (EI) mass spectrum fragment ion at *m*/*z* 436.3 corresponding to the formula $C_{28}H_{30}O_4$, further peak was observed at *m*/*z* 418.3, 403.3 and 267, respectively. Unsaturated δ-lactone A and B α, β with an intense band at 222 nm was characterized through UV spectrum and supported by IR spectrum, which indicated absorption band at 1698, 1710 and 3500 cm^{-1} for a six membered cyclic kentone α, β-unsaturated δ-lactone and hydroxyl group. The ^{1}H-NMR spectrum of **WTH2** has close resemblance to **WTH1**, indicating the same substitution in ring A, and B side. Instead of a double bond at C-4 and ether bridge substituted at C 14/20 compound **WTH2** in view of the shape of the signal of the 22-H, and while, its position also indicated the absence of a C-17-OH according to the molecular ion in the mass spectrum. The ^{1}H-NMR spectral data of **2** displayed five methyl signals at δ 1.38 (3H, s, CH_3-18) and δ 1.26 (3H, s, CH_3-19), δ 1.40 (3H, s, CH_3-21), δ 1.98 (3H, s, CH_3-27), δ 1.85 (3H, s, CH_3-28). A downfield double doublet at δ 4.34 (1H, $J_{22\alpha,23\alpha}$, = 12.7 Hz, $J_{22\alpha,23\beta}$ = 3.4 Hz, H22). The multiplicity of H-22 indicated the absence of proton attached to vicinal C-20.[22] Assignments of all functionality were achieved by HMBC and HMQC. The HMBC spectrum the 19-Me (δ 1.26), showed long range couplings (^{3}J) with C-1 (δ 203.4), C-5 (δ 136.4), and C-9 (δ 37.1). Similarly, ^{3}J the epoxy-bearing C-14 quaternary carbon (δ 84.4) showed ^{3}J coupling with the 17 methine and 18-methyl protons. Likewise, 3H-21 showed ^{2}J and ^{3}J coupling with C-20 (δ 76.2) and C-17 (δ 50.3), respectively (Fig. 8). This spectroscopy data led to the structure for **WTH2**. The structural and spectroscopic data of compound **WTH2**, including ^{1}H and ^{13}C NMR, DEPT experiments, 2D NMR (HSQC, HMBC, COSY, NOESY) for detailed proton-carbon connectivity and spatial correlations, along with GC-MS analysis illustrating the molecular ion peak and fragmentation patterns, are provided in the SI (Fig. S5–S8).

3.3. Spectral identification of the compounds

^{13}C-NMR (100 MHz) spectra were recorded in CD_3OD solution on a Bruker AV-500. 2D NMR spectra were recorded on a Bruker AMX 500 NMR spectrometer. EI-MS were recorded at 70 eV on a Finnigan MAT-112 or MAT-312 mass spectrometers. Chemical shifts are reported in ppm (δ), using CD_3OD. The recycling HPLC (JAI, LC-908W, Japan Analytical Industry Co. Ltd) was used for final purification with ODS H-80 or L-80 columns (YMC, Japan).

3.4. Enzyme inhibition activities

The enzyme inhibition effects of various extracts from *W. coagulans* on different health-related issues, are systematically detailed in the Table 2. *W. coagulans* extracts were evaluated for their inhibitory effects on enzymes related to neurological disorders, inflammation, diabetes, and skin conditions. The methanol extract displayed robust anti-inflammatory properties through strong lipoxygenase inhibition (144.76 mg QE per g extract), and it also showed significant inhibitory activity on AChE (4.10 mg GALAE per g extract) and BChE (3.71 mg GALAE per g extract), enzymes linked to neurological health. Ethyl acetate (EA) extract exhibited the highest glucosidase inhibition (3.51 mmol ACAE per g extract), suggesting its potential application in diabetes management, while *n*-butanol extract was notable for its high BChE inhibition (3.84 mg GALAE per g

Table 2 Enzyme inhibition effects of tested extract/fractions of *Withania coagulans*[a]

	Neurological problems		Inflammation	Diabetes	Skin problems
Extracts/fractions	AChE inhibition (mg GALAE per g extract)	BChE inhibition (mg GALAE per g extract)	Lipoxygenase (mg QE per g extract)	Glucosidase (mmol ACAE per g extract)	Tyrosinase (mg KAE per g extract)
Methanol	4.10 ± 0.91	3.71 ± 1.03	144.76 ± 2.13	1.94 ± 0.79	0.68 ± 0.68
n-Hexane	2.41 ± 1.31	1.70 ± 0.67	124.99 ± 1.14	1.87 ± 1.92	0.65 ± 1.13
Chloroform	3.51 ± 1.72	2.91 ± 1.12	97.63 ± 0.41	2.11 ± 0.67	0.83 ± 0.91
EA	3.91 ± 0.58	3.14 ± 1.42	137.84 ± 0.57	3.51 ± 0.52	0.18 ± 0.41
n-Butanol	2.87 ± 0.17	3.84 ± 0.41	129.04 ± 0.81	2.61 ± 1.12	0.94 ± 1.31

[a] GALAE: galatamine equivalent; QE: quercetin equivalent; ACAE: acarbose equivalent; KAE: kojic acid equivalent. All values expressed are means ± S.D. of three parallel measurements. Data marked with different letters within the same column indicate statistically significant differences for each species ($p < 0.05$).

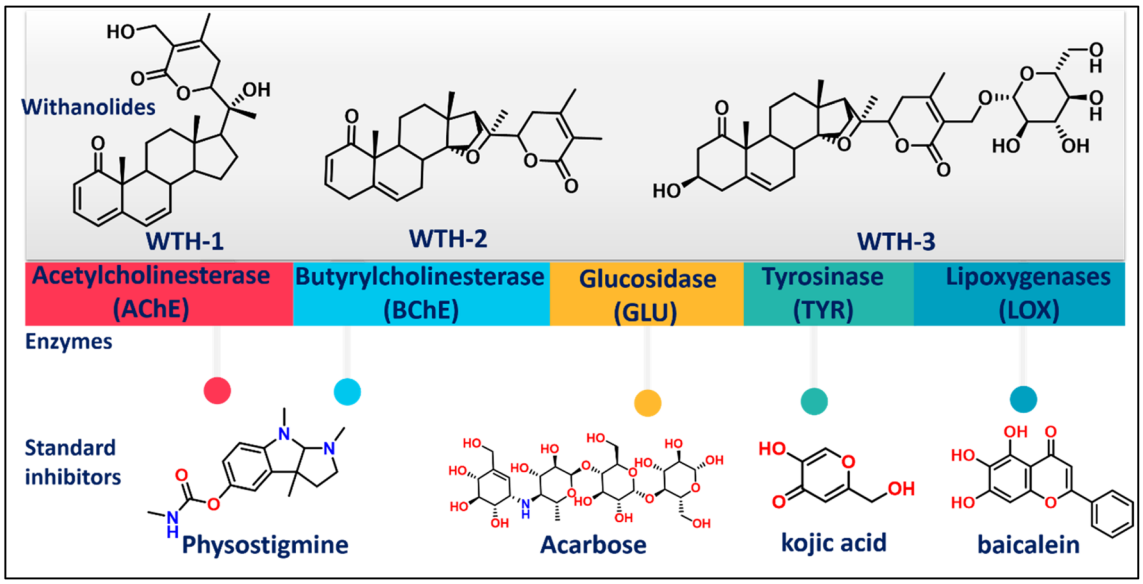

Fig. 2 Chemical structures of the isolated phytoconstituents and the benchmark inhibitors of enzymes under study.

extract) and the greatest tyrosinase inhibition (0.94 mg KAE per g extract), indicating its possible effectiveness in treating skin pigmentation disorders.

The findings highlight the complex interactions between the chemical profiles of *W. coagulans* extracts and their potential therapeutic applications. The varied enzyme inhibitory activities demonstrate the necessity for targeted research and development to optimize extraction methods that maximize health benefits, particularly for inflammation, neurological disorders, diabetes, and skin health. The correlations between bioactive content and biological activity also provide valuable insights, suggesting areas for further research in the extraction and application of natural products for health interventions.

3.5. Molecular docking studies

The binding mode of compounds (**WTH1**, **WTH2** and **WTH3**) (isolated by chromatographic analysis of *W. coagulans*) with the enzymes AChE, BChE, GLU, TYR, and LOX was investigated through molecular docking studies as shown in Fig. 2. Since, the *Saccharomyces cerevisiae* alpha-glucosidase (GLU) has not yet been reported on RCSB protein data bank, the most accurate phyre2 predicted structure for GLU was chosen, with a 93% confidence level. According to the Ramachandran plot, 99.2% of the residues have good *Z*-score values of −10.58, placing them in the favorable area. These findings validate the accuracy and dependability of the glucosidase protein model that was built.

In the case of AChE, the binding scores of the compounds ranged from −8.410 to −11.616 kcal mol^{-1}, whereas the standard compound (physostigmine, PHY or eserine) scored −5.85 kcal mol^{-1}. The **WTH1**, **WTH2** and **WTH3** have docking score −11.616, −8.410 and −11.438 respectively. The **WTH1** has highest binding affinity with AChE. The BChE binding scores of the compounds ranged from −5.144 to −8.615 kcal mol^{-1}, whereas the standard compound PHY scored −5.87 kcal mol^{-1}. **WTH3** demonstrated the highest binding affinity among the analyzed compounds, with a score of −9.30 kcal mol^{-1}. The **WTH1** and **WTH2** have docking score −5.144 and −6.167 kcal mol^{-1} respectively. For alpha-glucosidase (GLU), the docking scores of the compounds ranged from −2.986 to −7.267 kcal mol^{-1}. The **WTH3** docking score −7.267 kcal mol^{-1} was comparable to that of the standard inhibitor ACB (−8.891 kcal mol^{-1}). On other hand **WTH1** and **WTH2** have docking score −3.973 and −2.986 kcal mol^{-1} respectively. Apart from GLU enzyme, **WTH1** also demonstrated highest binding affinity towards TYR enzyme (−5.042 kcal mol^{-1}). Whereas, the standard inhibitor KJC also showed comparable binding potential (−6.81 kcal mol^{-1}). The **WTH2** and **WTH3** have docking score −4.543 and −4.696 respectively for TYR. The docking scores of the compounds in LOX-bonded systems ranged from −5.867 to −6.139 kcal mol^{-1}. With a highest docking scores of −6.139 kcal mol^{-1}, **WTH1** displayed significant binding potential towards LOX. The docking scores of the standard compound was −6.53 kcal mol^{-1}, which is comparable to **WTH3**. **WTH2** and **WTH3** have docking score −5.922 and −5.867 kcal mol^{-1} which is also comparable to the standard baiclain docking score −6.53 kcal mol^{-1} as shown in Table 3. These findings clearly indicate that among isolated compounds **WTH1**, **WTH2** and **WTH3** are the main active ingredients responsible for the enzyme inhibitory potential of *W. coagulans*.

To elucidate the variances in docking scores resultant from diverse interaction modalities, the optimal docking configurations for each molecule were documented and depicted graphically (Fig. 3). All ligands, along with benchmark inhibitors, occupy the same binding pocket. The graphical representation discloses that the AChE-ligand complexes share common interacting residues D72, Y70, Y121, W279, F290, F288, I287, and Y334 as demonstrated in (Fig. 3 superpose). In contrast, the AChE-PHY complex interacts with a distinct set of residues, including Q74, R289, F290, Y121, S286, and Y70, as illustrated

Table 3 Docking score of standard AChE, BChE (physostigmine), GLU (acarbose), TYR (kojic acid), LOX (baicalain)

Docking scores (kcal mol^{-1})					
Compounds	AChE	BChE	GLU	TYR	LOX
Standard	−5.85	−5.87	−8.89	−6.81	−6.53
WTH1	−11.616	−5.144	−3.973	−5.042	−6.139
WTH2	−8.410	−6.167	−2.986	−4.543	−5.922
WTH3	−11.438	−9.30	−7.267	−4.696	−5.867

in (Fig. 3 Image standard inhibitor). Furthermore, AChE and the three ligands integrate profoundly within the dual sub-sites (CAS and PAS) of AChE main active site. In the AChE-**WTH1** complex, the binding involves key residues Y72, T83, W86, W286, F297, Y337, V294, F338, Y133, E202, and F295. **WTH1** binds tightly through key hydrogen bonds with E202, Y72, and F338 (Image AI) and enhances hydrophobic interactions *via* residues F295 and F297, contributing to its specificity and stability (Image AI, Fig. S1 Image A1). The pyran-2-one ring of **WTH1** penetrates deeply into the PAS region, where its hydroxyl group at the methyl-substituted carbon of the ring forms a hydrogen bond with the backbone oxygen of F338. Additionally, the hydroxyl group at carbon attach with ring D into the hydrophobic gorge between the CAS and PAS sub-sites, forming a hydrogen bond with the side chain hydroxyl group of Y72. The oxygen atom linked to the steroid backbone forms a hydrogen bond with the hydroxyl group of residues E202. PLIP analysis shows **WTH1** binds tightly to AChE with key hydrophobic interactions and multiple contacts, indicating high specificity and effective binding with distances between 3.10 to 3.93 Å. In AChE-**WTH2** bonded system have residues S81, W84, N85, H440, S122, Y121, F290, F288, F330, F331, H440, E199 and W279. It has one hydrogen bond with Y121 as shown in (Fig. 3 Image AII). The steroid backbone has oxygen atom make hydrogen bond with hydroxyl group of Y121. Residue F288, F290, F330, and F331, along with I287, strengthen the hydrophobic environment within the binding pocket. S81, S122, E199, and H440 play crucial roles in hydrogen bonding and ionic interactions, orienting the ligand for optimal inhibition (Fig. S1 Image B). **WTH2** exhibits a robust binding profile as an AChE inhibitor, characterized by strategic hydrogen bonding and extensive hydrophobic contacts with a tight ligand–protein fit indicated by distances ranging from 3.32 to 3.88 Å. In AChE-**WTH3** bonded system have residues W84, S286, F331, F330, H440, E199, S122, W279, S286, Y334, G335, Y121, I287, Y130 and S200. It has four hydrogen bonds, each H-bond bond with Y130, Y121, Y334 and G335 as shown in (Fig. 3 Image AIII). The hydroxyl group attach with steroid backbone make hydrogen

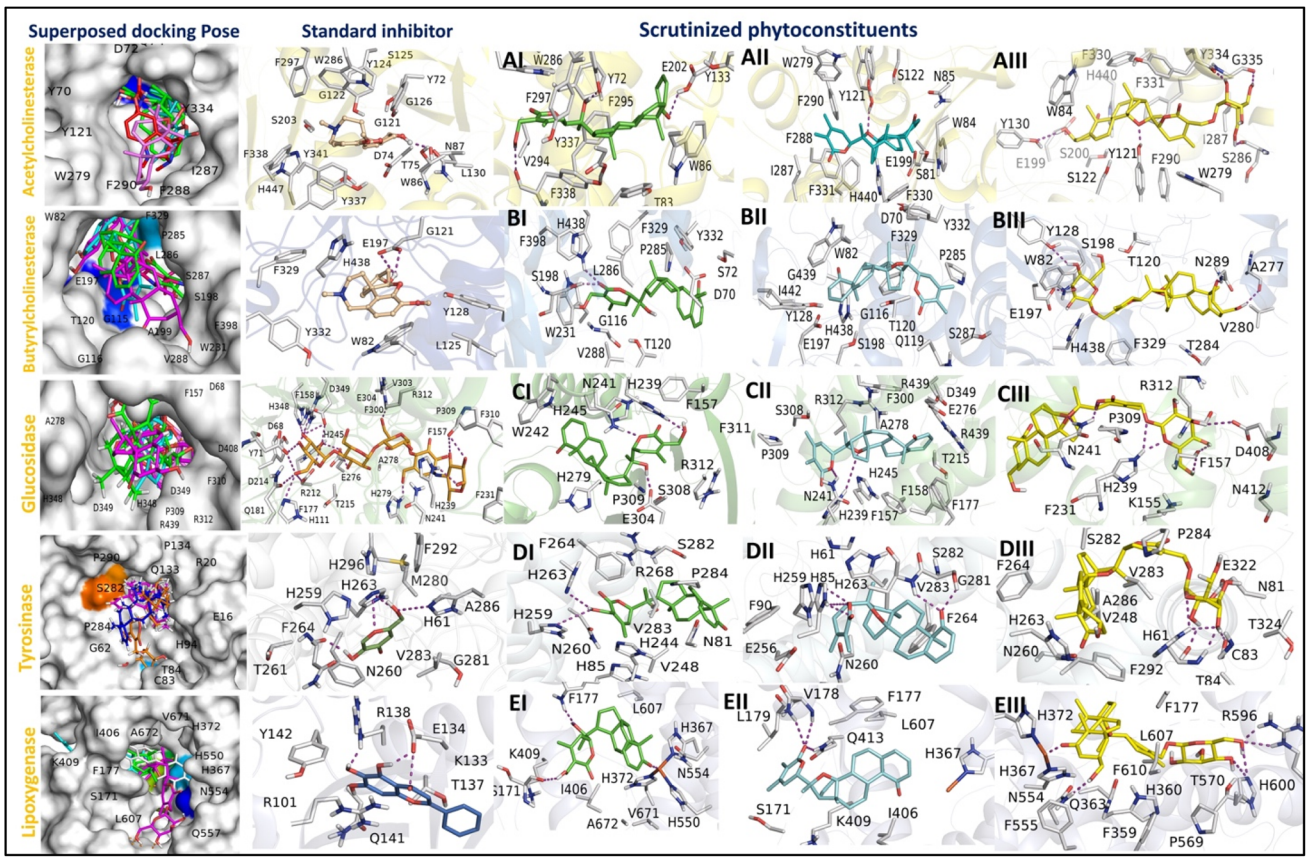

Fig. 3 Docking-generated complexes involving enzymes AChE, BChE, GLU, TYR, and LOX were superimposed with standard inhibitors and tested compounds. Complexes of proteins and their tested compounds: (AI) AChE-**WTH1** (AII) AChE-**WTH2** (AIII) AChE-**WTH3** (BI) BChE-**WTH1** (BII) BChE-**WTH2** (BIII) BChE-**WTH3** (CI) GLU-**WTH1** (CII) GLU-**WTH2** (CIII) GLU-**WTH3** (DI) TYR-**WTH1** (DII) TYR-**WTH2** (DIII) TYR-**WTH3** (EI) LOX-**WTH1** (EII) LOX-**WTH2** (EIII) LOX-**WTH3**.

bond with oxygen extended from hydroxyl group of Y130. The oxygen present in the ring D of steroid backbone also make hydrogen bond with oxygen extended from hydroxyl group of Y121. The hydroxyl groups of lactone group attach with the epoxide group make two hydrogen bond, one hydrogen bond with oxygen of aliphatic chain of Y334 and other hydrogen bond with oxygen of G335. In ACHE-**WTH3** interaction, aromatic residues such as W84, Y121, and F330 engage in both π–π stacking and hydrogen bonding, enhancing ligand affinity (Fig. S1 Image C). Notably, H440 s imidazole side chain might stabilize the ligand through possibly π interactions. These additional interactions resulting from the structure of the evaluated compounds account for the second higher docking score of **WTH3** compared to the **WTH1**. While PLIP interpret W279, L282, and F331 enhance ligand packing with hydrophobic interaction from 3.18 Å to 3.92 Å. AChE key residues G118, Y130, E199, S200, and D285 engage in hydrogen bonds ranging from 1.96 Å to 3.21 Å.

In BChE-ligand bonded systems, the residues surrounding the standard PHY and tested compounds are W82, S287, Y128, E197, G121, L125, H438, Y332 and F329 as shown in (Fig. 3 Image superpose). In BChE-PHY bonded system have residues W82, Y128, E197, A199, L286, V288, F398, W231, G115, T120, G115 and F329. In BChE-PHY bonded system, two hydrogen bonds with residue E197 (Fig. 3 Image standard inhibitor). In BChE-**WTH1** have residues L286, V288, F398, S198, H438, G116, L286, Y332, P285, F329, D70, W231, T120, and S72. The oxygen of pyran-2-one ring structure make one hydrogen bond with hydroxyl group of S198 and one hydrogen bond with nitrogen of H438 (Fig. 3 Image BI). Hydrophobic interactions with residues F329, Y332, D70, L286, G117, and V288 form a snug pocket around the ligand, facilitating van der Waals interactions as depicted in (Fig. S1 Image D). Using PLIP, BChE-**WTH1** interactions involve hydrophobic contacts with D70, G116, G117, L286, V288, F329, and Y332 ranging from 3.22 to 3.97 Å, and hydrogen bonds by G117 at 3.10 Å and 3.04 Å, S198 at 2.13 Å and 2.37 Å, and A199 at 3.18 Å, showing a tight fit and strong interactions in the binding site. H438 forms a salt bridge at 4.96 Å, highlighting precise ionic interactions with **WTH1**. In BChE-**WTH2** bonded system have various different residues Q119, S198, G439, T120, P285, and I442 (Fig. 3 Image BII). It has hydrophobic interaction with residues W82, Y332, Y128, G116, E197, I442 and H438. This complex has no hydrogen bonding with any residue as shown in SI (Fig. S1 Image E). The presence of an aromatic ring, likely that of Y332, is poised to contribute to potential π–π interactions, adding another layer of specificity and binding affinity to the ligand. PLIP analysis reveals that **WTH2** engages in key hydrophobic interactions with BCHE at 3.17 Å for W82 and 3.61 Å for Y332, and forms hydrogen bonds at 3.94 Å from W82 and 3.25 Å from G116, highlighting essential anchoring within the BCHE binding site. In BChE-**WTH3** bonded system have various different residues W82, Y128, E197, V280, A277, F329, N289, T120, S198, T284 and H438. **WTH3** has three hydrogen bonds, one hydrogen bond between hydrogen of one hydroxyl group of lactone ring and oxygen of hydroxyl group of Y128 and other hydrogen bond with other hydroxyl group of lactone ring and oxygen extended from residue E197 (Fig. 3 image BIII). The hydroxyl group of steroid backbone also make hydrogen bond with oxygen extended from residue A277. It also has hydrophobic interaction with residues W82, H438, F329 and E197 as shown in SI (Fig. S1 Image F). The indole ring of W82 are positioned to engage in stacking interactions, potentially stabilizing the ligand through π–π contacts. The network of surrounding residues, like T120, N289, and the aliphatic chains of A277 and V280, further sculpt the contours of this niche, possibly through hydrophobic contacts and van der Waals forces. PLIP analysis of the BCHE-**WTH3** complex shows hydrophobic contacts with D70, T120, A277, S287, and F329 ranging from 3.37 Å to 3.79 Å, supporting ligand-binding pocket formation, and details hydrogen bonds from G116, T120, G121, Y128, E197, A277, and S287 between 1.96 Å to 3.87 Å, highlighting critical stabilizing interactions within the protein structure.

In GLU the binding cavity consists of various residues, including D68, D349, A278, D349, P309, F310, R312, H348, F157, R439 and F157 (Fig. 3 Image superpose). In GLU-Acarbose system have different residues from superpose docking are N241, F300, Q181, E276, H111, D214, F231, H239, H279, and F177. It has approximately 15 hydrogen bonds with the surrounding residues, including D214, D68, H111, H239, H279, E304, E276, P309, R212, H348, D349 and F158. There are two hydrogen bonds with each residue D68, D214 and E276 (Fig. 3 Image standard inhibitor). In GLU-**WTH1** have residues H239, N241, W242, R312, S308, P309, E304, H279, F157, F311 and E304. It has three hydrogen bonds, one hydrogen bond between methyl–hydroxyl group of pyran-2-one ring and nitro group of H239, second hydrogen bond between oxygen of pyran-2-one ring and nitro group of N241. The **WTH1** hydroxyl group at carbon attach with ring D of steroid backbone make hydrogen bond with extended oxygen of E304 (Fig. 3 Image CI). It has hydrophobic interaction with N241, H245, W242 and H279 as shown in SI (Fig. S1 Image G). The arrangement of aromatic rings, particularly the ring of H245 and H279 possibly stabilizing the ligand through π–π contacts. Hydrophobic contacts between N241, W242, and P307 with the ligand range from 3.46 to 3.94 Å, while hydrogen bonds with Q239 and G304 measure 2.16 Å and 1.68 Å, respectively, with a notable 167.09° donor angle for Q239. Additionally, a salt bridge with H253 at 4.30 Å enhances electrostatic complementarity with **WTH1**. In GLU-**WTH2** have residues A278, S308, H239, H245, E276, F177, F157, R439, F300, P309, N241, H239, F158, T215, D349 and R312. It has one hydrogen bond with H239 (Fig. 2 Image CII). The steroid backbone ring D have oxygen atom make hydrogen bond with nitro group of H239. It has hydrophobic interaction with residues H245, R439 and R312 as shown in SI (Fig. S1 Image H). Additionally, other residues such as S308, P309, N241, H239, D349, E276, and T215 in proximity to the ligand, which may also play roles in binding through various interactions like van der Waals forces or additional hydrogen bonds. Hydrophobic contacts with F157 and A278 at around 3.5 Å, hydrogen bonds with N241 and E276 showing distances of 2.91 Å and 3.20 Å and angles above 106°, and a salt bridge with H239 at 3.47 Å collectively stabilize the ligand within the binding site. In GLU-**WTH3** have residues P309, R312, D408, N412, F157,

K155, H239, N241 and F231. It has six hydrogen bonds with various residues two hydrogen bonds with H239, one hydrogen bonds with N241, two hydrogen bonds with F157 and one hydrogen bond with D408 (Fig. 3 Image CIII). The lactone ring attaches with epoxide group make four hydrogen bonds, two hydrogen bond with oxygen of F157, one hydrogen bond with oxygen of D408 and oxygen present within the lactone ring make hydrogen bond with nitrogen of H239. The oxygen between lactone and epoxide group also make hydrogen bond with nitrogen of H239. It also has hydrophobic interactions with residues W242, F231, and R312 as shown in SI (Fig. S1 Image I). Hydrophobic interactions with P231A at 3.81 Å, W242A at 3.70 Å, and R312A at 3.91 Å suggest effective ligand packing, while hydrogen bonds with L155A at 3.03 Å, F157A at 1.99 Å, N241A at 2.65 Å, R312A at 2.43 Å, and D408A at 2.51 Å enhance the specificity and stability of ligand–protein binding.

In TYR, the binding cavity of kojic acid-tested compounds have common residues, including P134, Q133, R20, E16, H94, T84, C83, G62, P284, S282 and P290 (Fig. 3 image superpose). There are residues F264, H61, T261, M280 and A286 in the binding cavity standard TYR-kojic acid different from binding cavity of other compounds (Fig. 3 Image standard inhibitor). It has four H-bonds, two H-bonds with H263 and one H-bond with each residue, one H-bond with F264 and one with A286. In TYR-**WTH1** bind cavity has residues H85, N81, P284, S282, H263, H259, F264, N260, V283, H244, V248 and R268. It has two hydrogen bonds, one with H259 and other hydrogen bond with H263 (Fig. 3 Image DI). Hydrogen bonds between the nitrogen in the imidazole ring of H263, H239 and a methyl–hydroxyl group pyran-2-one ring of **WTH1**. It also has hydrophobic interaction with H85, H244, P284 and F264 as shown in SI (Fig. S1 Image J). Hydrophobic interactions with H263, F264, and V283 range from 3.51 to 3.82 Å, stabilizing the complex through nonpolar contacts, while H263 forms a hydrogen bond at 2.56 Å and a 112.54° angle and a salt bridge at 5.32 Å, underscoring strong directional and electrostatic interactions that enhance binding specificity. In TYR-**WTH2** has common residues F90, H61, H85, H259, S282, H263, V283, G281, N260, E256 and F264. It has five hydrogen bonds, three H-bonds with H85 and one H-bond with V283 and one H-bond with G281 (Fig. 3 Image DII). The oxygen of ring A makes two hydrogen bonds, one H-bond with nitrogen of V283 and other with hydroxyl group of G281. The oxygen within the ring of pyran-2-one make two hydrogen bonds with H85. The oxygen extended from epoxide group also make H-bond with H85. It also has hydrophobic interaction with N260, H263, H259, F264 and H61 as shown in SI (Fig. S1 Image K). Residue F90, F264 and V283 are likely the key players in the hydrophobic interactions. F264 has a bulky, nonpolar benzyl side chain, which can engage in van der Waals forces with hydrophobic regions on the ligand. V283 with its smaller aliphatic side chain, also contributes to the hydrophobic contact points. The TYR-**WTH2** interaction includes hydrophobic contacts with H85A, E256A, N260A, H263A, and V283A between 2.74 and 3.47 Å, and hydrogen bonds by S282A at 2.21 Å and V283A at 2.45 Å, enhancing specificity and affinity. Salt bridges with H61A and H85A further stabilize the complex through electrostatic interactions. In TYR-**WTH3** have residues F264, S282, P284, V283, A286, V248, H263, N260, F292, H61, T84, C83, T324, N81 and E322. It has five hydrogen bonds, two hydrogen bonds with H61, Two H-bonds with T84 and one hydrogen bond with C83 (Fig. 3 Image DIII). The imidazole side chain of H61 make two hydrogen bonds, one H-bond with oxygen within the lactone ring and other H-bond with hydroxyl group of lactone ring. T84 and C83 make H-bond with same hydroxyl group of lactone ring and oxygen T84 make another hydrogen bond with other hydroxyl group of lactone ring. It has hydrophobic interaction with resides A286, F264, F292, H263, P284, V286 and V283 as shown in SI (Fig. S1 Image L). The TYR-**WTH3** complex features hydrophobic interactions with N260A, H263A, P264A, and V283A ranging from 3.23 Å to 3.78 Å for a tight ligand fit, and strong hydrogen bonds with A81A and C83A at 2.53 Å and 1.84 Å, respectively.

In the LOX binding cavity of Baicalain-compound have common residues including V671, S171, H372, H550, H367, N554, Q557, L607, F177, K409, I406 and A672 (Fig. 3 Image superpose). In LOX-Baicalain binding cavity have residues Q141, R138, R101, Y142, E134, K133 and T137. It has three hydrogen bonds one hydrogen bond with R138 and two hydrogen bonds with E134 (Fig. 3 Image standard inhibitor). In LOX-**WTH1** have residues different from standard binding cavity are K409, A672, V671, H372, H550, H367, N554, I406, S171 and L607. It has three hydrogen bond, one hydrogen bond with H367, one hydrogen bond with F177 and one bond with S171 (Fig. 3 Image EI). The methyl-hydroxyl group of pyran-2-one ring make hydrogen bond with extended oxygen from S171. The hydroxyl at carbon attach with ring D of **WTH1** make hydrogen bond with nitrogen of F177. It has hydrophobic interaction with the L607, F177, I406 and V671 which collectively create a nonpolar environment that helps secure the ligand in place through van der Waals forces. In the LOX-**WTH1** complex, the hydrophobic interactions are delineated by the binding of F177 (2.94 Å), K409A (3.64 Å), and L607 (3.41 Å), which anchors the ligand within the hydrophobic core of the protein. In LOX-**WTH2** binding cavity have residues L179, V178, L607, F177, Q413, H367, K409, I406 and S171. It has three hydrogen bonds, one hydrogen bond with Q413, two hydrogen bond with V178 and one bond with L179 (Fig. 3 Image EII). The nitrogen of V178, Q413 and L179 make hydrogen bond with oxygen extended from pyran-2-one ring. It has hydrophobic interaction with residues F177, I406, Q413 and V178. All residues present nonpolar side chains that interact with the hydrophobic parts of the ligand as shown in (Fig. S1 Image N). In the LOX-**WTH2** complex, hydrophobic interactions with P177, L179, I406, and L607 range from 3.25 Å to 3.61 Å, securing the ligand in a stable, nonpolar region. Hydrogen bonds by V178, L179, and Q413, ranging from 2.58 Å to 2.70 Å with angles up to 163.83°, enhance specificity and affinity for the LOX enzyme. In LOX-**WTH3** have residues H372, H367, Q363, N554, F555, H360, P569, T570, H600, R596, L607, F177, F610 and F359. It has six hydrogen bonds, two hydrogen bonds with R596, two hydrogen bonds with H600, one hydrogen bond with H367 and one hydrogen bond with Q363 (Fig. 3 Image EIII). The methyl–hydroxyl group of lactone ring make three hydrogen bonds, two hydrogen bonds with two nitrogen of R596 and

Table 4 ADME pharmacokinetic properties of the isolated compounds

Molecule	TPSA	Silicos-IT $\log S_w$	GI (% absorbed)	(SP) $\log K_p$ ($cm\ s^{-1}$)	BBB permeant	Pgp substrate	1A2 inhibitor	2C19 inhibitor	2C9 inhibitor	2D6 inhibitor	3A4 inhibitor	Bioavailability	Synthetic accessibility	TC (log ml min^{-1} kg^{-1})	AMES toxicity	MTDH (log mg per kg per day)	LD_{50} (mol kg^{-1})	Hepatotoxicity	MT (log mM)
WTH1	83.8	−3.84	97.67	−6.06	No	Yes	No	No	Yes	No	Yes	0.55	6.47	0.473	No	−0.664	2.24	No	0.149
WTH2	52.6	−5.62	98.06	−5.8	Yes	No	No	No	Yes	No	No	0.55	6.59	0.31	No	−0.406	1.83	No	0.272
WTH3	175.5	−3.81	94.56	−9.79	No	Yes	No	No	No	No	No	0.17	8.09	0.452	No	−0.685	2.14	No	0.146

other hydrogen bond with nitrogen of H600. Other hydroxyl attaches with lactone ring also make hydrogen bond with nitrogen of H600. The oxygen attach with ring A of steroid backbone makes hydrogen bond with oxygen attach with H367 and H372. The hydroxyl group attach with ring A of steroid backbone makes hydrogen bond with Q363. Meanwhile, the ligand is also ensconced within a hydrophobic pocket, with F177, F359, F610, L607, and P569 as shown in (Fig. S1 Image O) contributing to a nonpolar environment. In the LOX-**WTH3** complex, P177, I406, A410, and L607 engage in hydrophobic interactions, anchoring the ligand with distances between 3.34 Å to 3.90 Å. Hydrogen bonds are formed with N554 and R596 at distances as close as 2.09 Å, and with H600 at 2.09 Å, establishing tight, specific contacts critical for stable ligand binding.

3.6. Toxicological modelling and ADME profiling

The comprehensive analysis, detailed in Table 4, represents the ADME properties, physicochemical characteristics, pharmacological toxicity, mutagenesis profile, and synthetic accessibility for the compounds evaluated in our study. Most of the compounds exhibit synthetic accessibility scores under 5 which demonstrates the ease of developing them in practice. **WTH1** and **WTH2** achieve scores of 6.47 and 6.59 indicating they have easier synthetic pathways than **WTH3** which scores 8.09. This discrepancy can be attributed to the smaller molecular structure of **WTH1** and **WTH2**. Furthermore, **WTH1**, **WTH2**, and **WTH3** show impressive intestinal absorption rates 97.67%, 98.06% and 94.56% of respectively, highlighting their potential for effective gastrointestinal uptake. The absorption rate of **WTH2** reaches up to 98.06% which indicates superior bioavailability. The main enzymes responsible for processing these compounds are cytochrome P450 enzymes with emphasis on CYP2C9 because this enzyme plays an essential part in drug breakdown and elimination processes. Pharmacokinetic parameter total clearance gives essential information when determining the correct dosage to reach therapeutic concentrations by using log (ml min^{-1} kg^{-1}) units. The metabolic profiles indicate that CYP3A4 takes part in drug transformations which means drug interactions could occur. **WTH1** reaches 0.473 log ml min^{-1} kg^{-1} total clearance ranking first while **WTH3** and **WTH2** show respective second and third-place clearances at 0.452 log ml min^{-1} kg^{-1} and 0.31 log ml min^{-1} kg^{-1}. Through the pkCSM web platform and similar tools researchers generated ADME data about the pharmacokinetic characteristics of these compounds for evaluating their therapeutic value. The LD_{50} value of **WTH1** is 2.24 (mol kg^{-1}) which is greater than **WTH2** and **WTH3** value are 1.83 and 2.14 (mol kg^{-1}). The maximum recommended tolerated dose (MRTD) provides an estimate of the toxic dose threshold of compounds in humans. The MRTD of less than or equal to 0.477 log (mg per kg per day) is considered low and high if greater than 0.477. The maximum tolerated dose of humans (MTDH) of **WTH2** is −0.406 log (mg per kg per day) which is close to the recommended value but **WTH1** and **WTH3** value of MTDH is −0.664 and −0.685 log (mg per kg per day) respectively, which is greater than recommended dose. Pharmacokinetic analysis through ADME

assessment provides comprehensive data about examined compounds which identifies improvements that could enhance their therapeutic applications. The extensive ADMET characteristics of **WTH1**, **WTH2**, and **WTH3** combined with results from our extensive research serve as a solid basis to develop these compounds for future drug development phases that focus on formulation creation and usage evaluation.

3.7. DFT and MESP studies

The Molecular Electrostatic Potential (MESP) mappings have provided a comparative analysis of the electronic characteristics of AChE inhibitors, particularly focusing on three notable compounds: **WTH1**, **WTH2**, and **WTHA**. As depicted in Fig. 4, these mappings highlight the distinctive electronic properties that contribute to unique biochemical interactions with AChE. The analyses were conducted in aqueous environments to assess the CNS-related neuroprotective effects of all compounds under physiological conditions, offering a relevant scenario for the evaluation of these potential therapeutics. The MESP mappings accentuate regions of high electronegative potential, marked by a deep red color across all three structures. The identified essential regions show optimal conditions for electrophilic connections needed for powerful binding with subsequent AChE inhibition. At position 28 in **WTH1** the oxygen atom has been identified through Mulliken population analysis to hold an exceptionally negative charge equalling −0.58. The MESP map shows the highest red intensity zone where this interaction would occur. A similar trend is noted in **WTH2**, where oxygen at position 27 exhibits a Mulliken charge of −0.59, enhancing its potential for hydrogen bonding within the strategic hinge and solvent-exposed regions of AChE. **WTH3** also features a negatively charged region at oxygen position 39 with a Mulliken charge of −0.57, furthering its capability to form hydrogen bonds with AChE. Notably, **WTH2** displays more neutral areas (shown in green), suggesting a propensity for hydrophobic or van der Waals interactions, whereas **WTH3** shows a balanced representation of both red and green areas conducive to diverse interaction types.

The reactivity of the compounds is strongly dependent on this analysis. This is especially true for the HOMO–LUMO

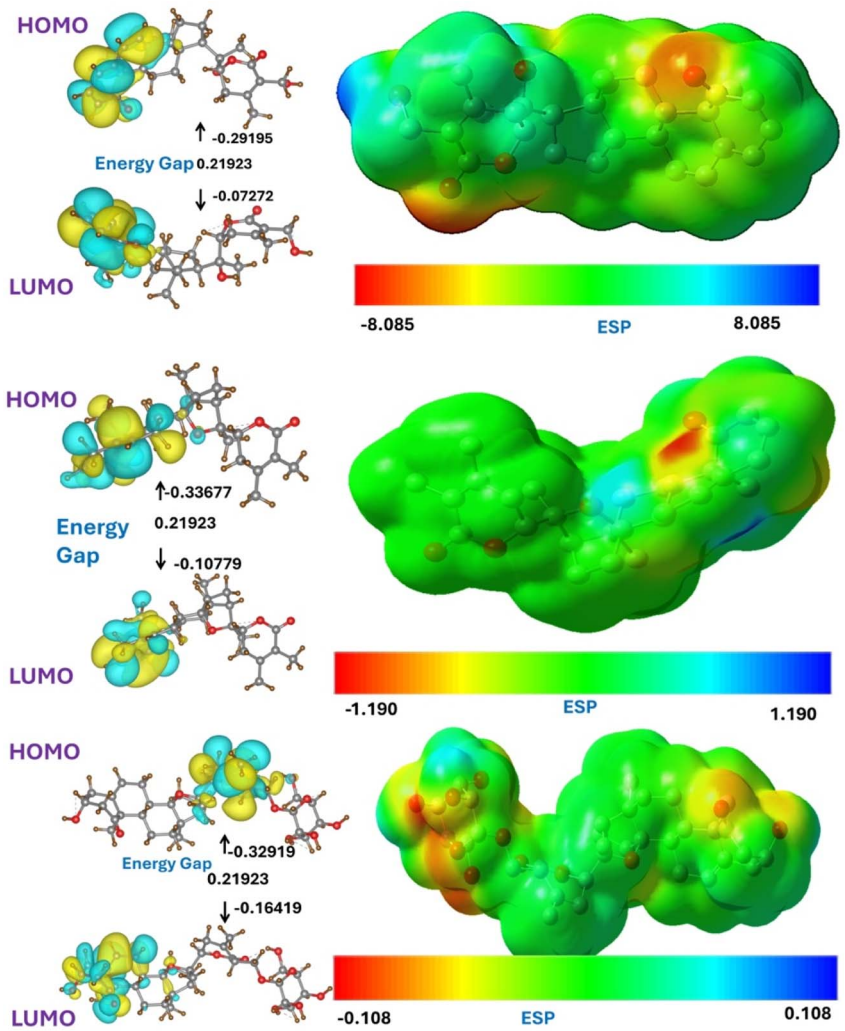

Fig. 4 ESP structures (in solvent phases) formed by mapping of total density over electrostatic potential, and optimized structures WTH1, WTH2, WTHA. Calculated HOMO and LUMO orbitals of potent derivatives at B3LYP/SVP level of DFT calculations for all selected ligands.

Table 5 DFT analysis of the isolated compounds

Parameters for DFT analysis											
Ligand	Dipole moment (debye)	HOMO (a.u.)	LUMO (a.u.)	Energy gap (ΔE_{Gap})	Ionization potential (eV)	Electron affinity (eV)	Electronegativity χ (eV)	Electrochemical potential μ (eV)	Hardness η (eV)	Softness S (eV)	Electrophilicity ω (eV)
WTH1	2.0757	−7.944	1.979	9.923	7.944	−1.979	2.983	−2.983	9.923	0.101	0.448
WTH2	6.0750	−9.164	2.933	12.097	9.164	−2.933	3.115	−3.115	12.097	0.083	0.401
WTHA	2.3116	−8.958	−4.468	4.49	8.958	4.468	6.713	−6.713	4.49	0.223	5.018

energy gap, which is the lowest unoccupied and highest occupied molecular orbital energy difference. It is this gap that is necessary to understand the energy transfer of the molecule to itself. In Fig. 4, the molecular surface plots of HOMO and LUMO orbitals are shown for **WTH1**, **WTH2** and **WTH3**. Contact values for the HOMO and LUMO indicate the compound's ability to accept or donate electrons. In Table 5, a summary is provided of the calculated quantum chemical descriptors for these compounds under aqueous conditions. DFT calculations have shed light on the AChE inhibitors' reactivity patterns and electronic structures. Notably, **WTH2** exhibited an extraordinarily high dipole moment of 6.0750 debye, indicating a distinct electronic profile compared to **WTH1** and **WTH3**, which demonstrated significantly lower dipole moments of 2.0757 and 2.3116 debye respectively. This suggests different electron-donating capabilities and interaction potentials with AChE. The HOMO–LUMO energy gap analysis revealed that **WTH2** also exhibited the largest disparity, signifying enhanced reactivity and potential biological efficacy. These findings not only deepen our understanding of the molecular basis for the inhibitory activity against AChE but also highlight the critical need to optimize electronic and structural properties for the development of potent AChE inhibitors. This detailed analysis sets the foundation for subsequent structure–activity relationship studies, which will guide the design of novel inhibitors with improved therapeutic profiles.

Employing Koopman's theorem, global reactivity parameters for ligands **WTH1**, **WTH2**, and **WTH3** have been computed, demonstrating notable differences in their electronic properties as depicted in the data. **WTH1** is characterized by an intermediate level of electronegativity ($\chi = 2.983$ eV) and chemical potential ($\mu = -2.983$ eV), with a substantial absolute hardness ($\eta = 9.923$ eV). The hardness obtained is very high and is consistent with a very strong resistance to deformation of the electron cloud, implying few degrees of freedom in adopting to changes in the electron distribution. This is further supported by its low global softness ($\sigma = 0.101$ eV^{-1}) and moderate electrophilicity index ($\omega = 0.448$ eV). On the other hand, **WTH2** shows slightly higher electronegativity ($\chi = 3.115$ eV), chemical potential ($\mu = -3.115$ eV) and hardness ($\eta = 12.097$ eV) among the ligands under consideration. This high hardness is comparable to a striking degree of resistance to electronic rearrangement, and is a function of the lowest global softness ($\sigma = 0.083$ eV^{-1}). As a result, **WTH2** presents a rather less propensity to accept electrons, as its electrophilicity index ($\omega = 0.401$ eV) suggests. Conversely, **WTH3** stands out with significantly higher electronegativity ($\chi = 6.713$ eV) and chemical potential ($\mu = -6.713$ eV), signaling a potent ability to attract electrons compared to **WTH1** and **WTH2**. It features the lowest hardness ($\eta = 4.49$ eV) among the ligands, which correlates with a higher global softness ($\sigma = 0.223$ eV^{-1}). This suggests a greater flexibility in its electron cloud, facilitating easier electron mobility. **WTH3** electrophilicity index ($\omega = 5.018$ eV) is notably the highest, indicating a pronounced ability to stabilize additional electron density and thereby enhancing its reactivity under electrophilic attack. These distinct parameters illuminate the underlying electronic behavior of **WTH1** and **WTH2** as more resistant to electron cloud deformation, while **WTH3** emerges as markedly adept at electron stabilization, presenting a stark contrast in reactivity profiles, which could influence their utility in various chemical environments.

3.8. Dynamic simulations, comprehensive analysis of structural flexibility and stability

In the current investigation, molecular dynamics (MD) simulations combined with free energy analyses were performed to scrutinize the binding modes and interaction mechanisms of the eserine inhibitor and **WTH1**, both targeting AChE with varying efficacies.[26,27] Importantly, **WTH1** exhibited an inhibitory capacity approximately slightly superior to that of eserine, as delineated in Fig. 5C, **WTH1** and eserine, underscoring three pivotal structural alterations that considerably enhance the AChE binding affinity of **WTH1** compared to eserine. These modifications encompass the replacement of the nitro group on the benzene ring, the integration of a pyra-2-one, and the substitution of both pyrole rings with a steroidal scaffold. Additionally, the interactions involving methyl and hydroxyl groups linked to the carbon between the pyra-2-one and the steroid backbone significantly contribute to the AChE binding. As Table 1 indicates, **WTH1** shows an enhanced potency compared to eserine, which shares some structural resemblances and similar AChE inhibitory activity. Fig. 5C and 4D show that docking studies show that the inhibitors adopt almost equivalent conformations in the AChE ligand binding pocket. According to these findings, **WTH1** and eserine were chosen for additional molecular dynamics (MD) simulation and binding free energy analyses to identify the major structural elements necessary for AChE inhibition, which will serve as a basis for the development of more potent AChE inhibitors.

The analysis of system dynamic stability included RMSD assessment from initial structures during 100 ns molecular

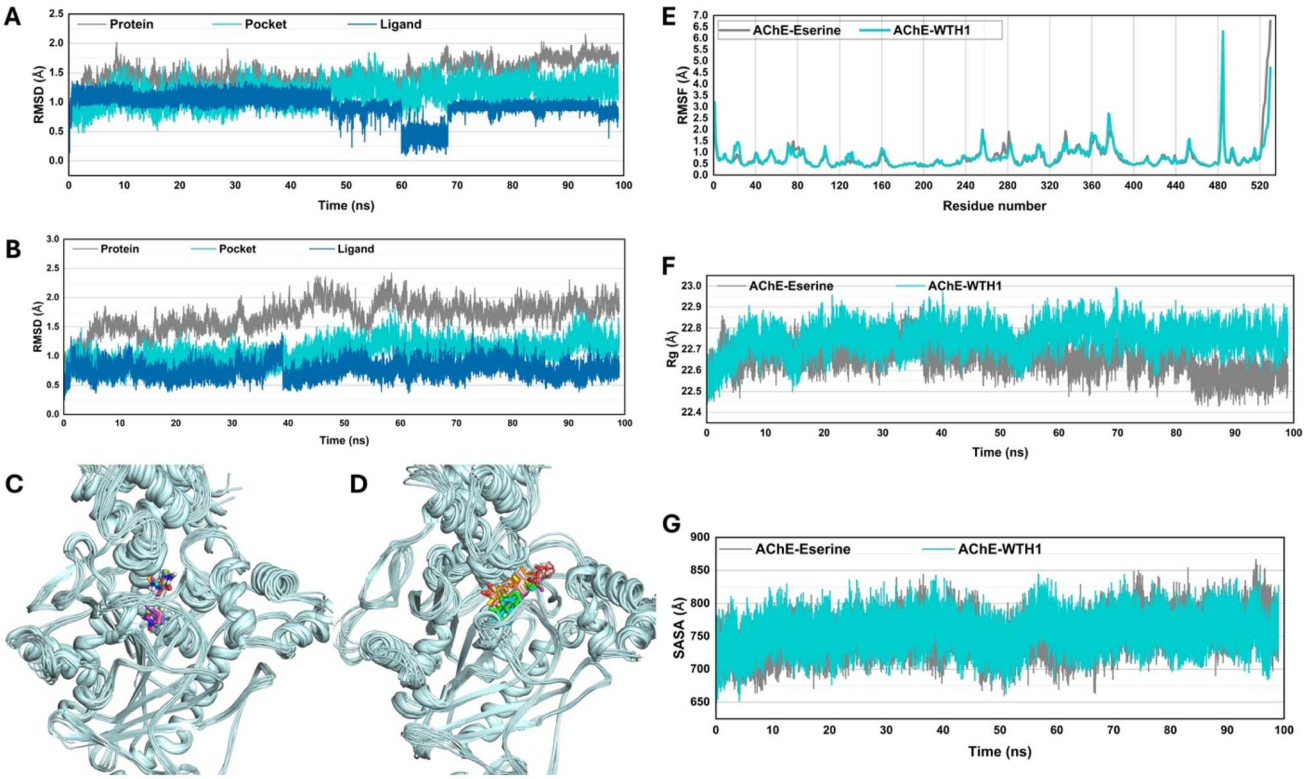

Fig. 5 (A and B) Root-mean-square deviation (RMSD) curve for AChE-**WTH1** and AChE-eserine structure (C) ligand binding cavity in AChE with **WTH1** and eserine (D) all selected ligands occupying the same binding site of AChE protein. (E) Root mean fluctuation (RMSF) curve for AChE-**WTH1** and their comparison to AChE-eserine structure. (F and G) Plots for radius of gyration (ROG) and solvent accessible surface area (SASA) for both complexes.

dynamics (MD) simulations to validate the sampling method. An RMSD analysis confirmed that the **WTH1**-AChE and eserine-AChE complexes plus all other simulation systems established equilibrium during the first 5 nanoseconds of the MD simulation. The equilibrium period for the simulations produced stabilized RMSD values amounting to 1.7 Å for protein Cα atoms, 1.0 Å for binding pocket backbone atoms and 0.8 Å for ligand heavy atoms. The visualization of stability results in Fig. 5A and B confirms the system stability which enables following analyses that depend on conformations sampled between 5 and 100 ns. Monitoring the structural stability used snapshot coordinates from the MD simulation which were superposed against initial structures as shown in Fig. 5C and D. MD simulation results showed that eserine- as well as **WTH1**-AChE complexes maintained structural stability throughout the simulation while both ligands kept their original positions by sustaining critical hydrogen bonds with PAS and CAS region residues. Our MD simulation results show high reliability because the obtained findings help explain inhibitor-AChE interaction mechanisms while preparing for binding free energy studies.

The root-mean-square fluctuation (RMSF) analysis encompassing all ligand–protein interactions, as depicted in Fig. 5E,

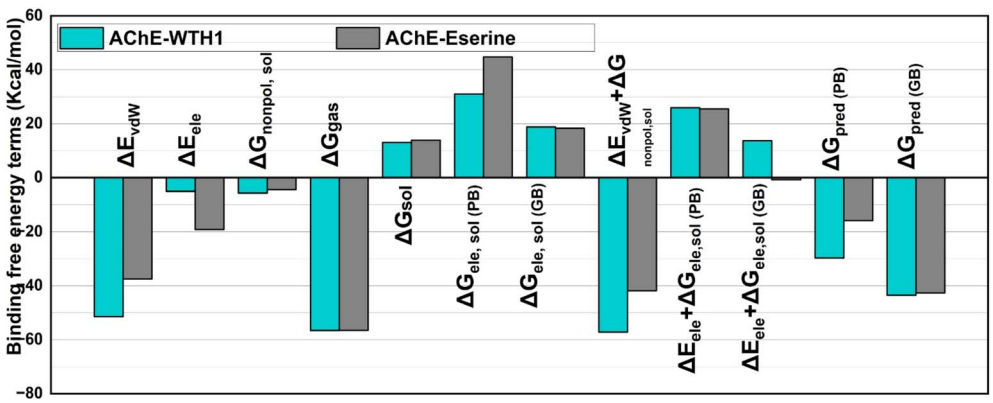

Fig. 6 Binding free energy (kcal mol^{-1}) terms of AChE-**WTH1** and AChE-eserine.

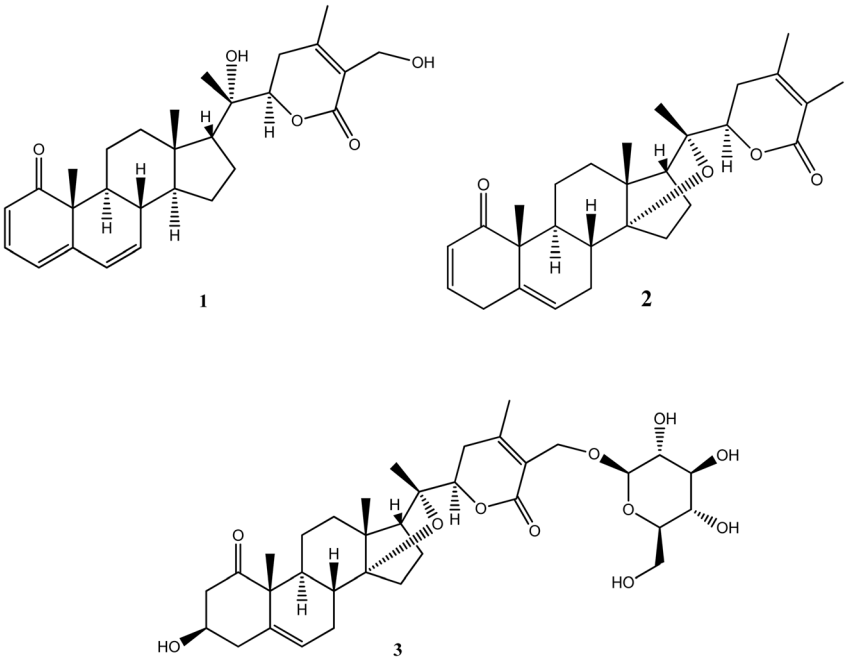

Fig. 7 Isolated new compounds **WTH1**, **WTH2** and known **WTH3**.

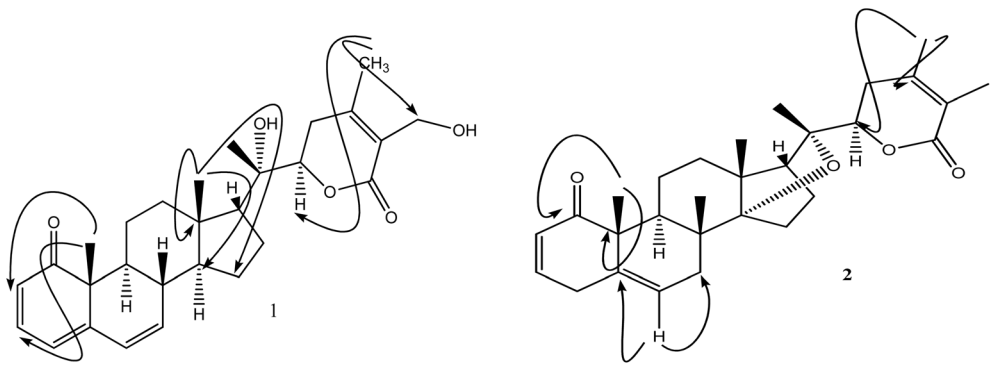

Fig. 8 Key correlation of HMBC compounds **1**, **2** (**WTH1**, **WTH2**).

delineates the dynamic profiles and RMSF distribution across the protein structures of all evaluated systems. These dynamics manifest consistent patterns, with three areas within the acetylcholinesterase (AChE) structure, the catalytic active site (CAS), peripheral anionic site (PAS), and Mid Gorge (situated between the CAS and PAS), displaying pronounced fluctuations. In particular, the CAS (residues 119–126 and 447–458) showed similar fluctuations in nonbonded and bonded interaction with AChE. However, in the systems on passive binding, the peripheral anionic site (PAS), which covers residues 72–76 and 280–290, had slightly higher fluctuations. These changes imply increased mobility of the Mid Gorge (residues 294–297) in the presence of AChE due to ligand binding and thus increased flexibility between the CAS and PAS regions. Additionally, residues 480–490 in the CAS region exhibited increased fluctuations in the AChE-eserine and **WTH1** complexes. Despite the variability, the Mid Gorge and PAS regions generally followed

Table 6 Binding free energy (kcal mol^{-1}) terms of AChE-**WTH1** and AChE-eserine

Complex	ACHE-**WTH1** (kcal mol^{-1})	ACHE-ESE (kcal mol^{-1})
ΔE_{vdW}[a]	−51.5212	−37.4592
ΔE_{ele}[a]	−5.1078	−19.1437
$\Delta G_{nonpol,sol}$[a]	−5.726	−4.4617
Δg_{gas}	−56.629	−56.6029
ΔG_{sol}	13.089	13.9041
$\Delta G_{ele,sol\ (PB)}$[a]	31.0876	44.6799
$\Delta G_{ele,sol\ (GB)}$[a]	18.8149	18.3657
$\Delta E_{vdW} + \Delta G_{nonpol,sol}$[a]	−57.2472	−41.9209
$\Delta E_{ele} + \Delta G_{ele,sol\ (PB)}$[a]	25.9798	25.5362
$\Delta E_{ele} + \Delta G_{ele,sol\ (GB)}$[a]	13.7071	−0.778
$\Delta G_{pred\ (PB)}$[b]	−29.731	−15.0831
$\Delta G_{pred\ (GB)}$[b]	−43.54	−42.6988

a similar fluctuation pattern, whereas AChE-eserine and **WTH1** complexes noted fluctuations in these loops. In contrast, the CAS, PAS, and Mid Gorge regions displayed stability across both AChE systems, underscoring their essential role in maintaining structural integrity upon ligand binding. Notably, the CAS residues in receptor–ligand bonded systems exhibited a heightened fluctuation amplitude relative to those in the nonbonded AChE configuration, highlighting the significant dynamic influence of ligand binding on the mobility of this critical region.

The radius of gyration (R_g) of AChE was measured throughout the simulation in order to gauge the effect of ligand binding on the structural integrity of the protein, as shown in Fig. 5F. About 22.6 Å and 22.7 Å average R_g values for AChE bound to eserine and **WTH1**, respectively, were found to be in reasonably good agreement. They serve as an indication that ligand binding does not activate significant structural change in

Table 7 New and known isolated compounds of *Withania coagulans*

	Compound **1**			Compound **2**			Compound **3**		
C no	δ_C	Multi	$\delta_H J$ in Hz	δ_C	Multi	$\delta_H J$ in Hz	δ_C	Multi	$\delta_H J$ in Hz
1	214.4	C	—	213	C	—	214.2	C	—
2	46.8	CH_2	2.74 (1H, m) 2.09 (1H, m)	47.2	CH_2	2.85 (1H, dd, J = 13.0, 9.9), 2.70 (1H, dd, J = 13.0, 5.7)	46.8	CH_2	2.72 (1H, d, J = 7.0) 2.00 (1H, m)
3	76.9	CH	4.00 (1H, m)	76.8	CH	3.88 (1H, m)	76.8	CH	4.00 (1H, m)
4	38.8	CH_2	2.68 (1H, dd, J = 6.2, 13.6) 2.45 (1H, d, J = 13.6)	38.8	CH_2	2.67 (1H, dd, J = 13.6, 5.8) 2.58 (1H, m)	38.8	CH_2	2.68 (1H, dd, J = 6.3, 13.6) 2.48 (1H, d, J = 13.6)
5	136.4	C	—	135.5	C	—	136.5	C	—
6	126.8	CH	5.69 (1H, br s)	127.4	CH	5.71 (1H, d, J = 5.2)	126.8	CH	5.67 (1H, br s)
7	26.6	CH_2	2.09 (2H, m)	27.5	CH_2	2.21 (1H, m), 1.81 (1H, m)	26.9	CH_2	2.10 (1H, m), 1.92 (1H, m)
8	35.4	CH	1.90 (1H, m)	38	CH	1.77 (1H, m)	37.1	CH	2.58 (1H, m)
9	37.4	CH	2.04 (1H, m)	39.5	CH	1.85 (1H, m)	37.1	CH	2.58 (1H, m)
10	54.3	C	—	54.1	C	—	54.3	C	—
11	22.3	CH_2	1.99 (1H, m) 1.54 (1H, m)	23.2	CH_2	1.68 (1H, m) 1.40 (1H, m)	23.2	CH_2	2.08 (1H, m) 1.64 (1H, m)
12	33.2	CH_2	2.01 (1H, m) 1.65 (1H, m)	34.6	CH_2	2.46 (1H, m) 1.66 (1H, m)	31.5	CH_2	2.34 (1H, ddd, J = 24.6, 12.6, 5.3), 1.27 (1H, m)
13	49.6	C	—	55.8	C	—	55.7	C	—
14	85.5	C	—	86	C	—	84	C	—
15	32.9	CH_2	1.94 (1H, m) 1.52 (1H, m)	32.1	CH_2	2.08 (1H, m), 1.49 (1H, m)	33.2	CH_2	1.74 (2H, m)
16	21.7	CH_2	1.89 (2H, m)	33.2	CH_2	2.47 (1H, m) 1.57 (1H, m)	37.5	CH_2	1.52 (1H, m) 1.48 (1H, m)
17	50.7	CH	2.30 (1H, t, J = 9.4)	89.2	C	—	88.8	C	—
18	18	CH_3	1.04 (3H, s)	17.9	CH_3	1.28 (3H, s)	21	CH_3	1.11 (3H, s)
19	18.5	CH_3	1.27 (3H, s)	19.6	CH_3	1.31 (3H, s)	18.8	CH_3	1.27 (3H, s)
20	76.5	C	—	79.2	C	—	79.9	C	—
21	20.2	CH_3	1.28 (3H, s)	17.8	CH_3	1.43 (3H, s)	19.5	CH_3	1.37 (3H, s)
22	83.2	CH	4.23 (1H, dd, J = 13.2, 3.4)	84.3	CH	4.58 (1H, dd, J = 13.2, 3.4)	83	CH	4.82 (1H, d, J = 3.4)
23	32.8	CH_2	2.51 (1H, dd, J = 18.0, 13.2) 2.39 (1H, dd, J = 18.0, 3.4)	35.2	CH_2	2.64 (1H, dd, J = 18.8,13.2) 2.47 (1H, dd, J = 18.8, 3.4)	35.7	CH_2	2.64 (1H, dd, J = 18.8, 13.2) 2.50 (1H, dd, J = 18.8, 3.42)
24	157.5	C	—	153.1	C	—	153.4	C	—
25	126.8	C	—	121.9	C	—	122	C	—
26	168	C	—	169	C	—	169.1	C	—
27	56.4	CH_2	4.38 (1H, d, J = 11.2) 4.30 (1H, d, J = 11.2)	12.3	CH_3	1.84 (3H, s)	12.3	CH_3	1.84 (3H, s)
28	20.2	CH_3	2.09 (3H, s)	20.5	CH_3	1.95 (3H, s)	20.5	CH_3	1.95 (3H, s)
1′	103.1	CH	4.36 (1H, d, J = 7.6)	102.9	CH	4.37 (1H, d, J = 7.8)	103	CH	4.35 (1H, d, J = 7.7)
2′	75.1	CH	3.13 (1H, dd, J = 7.8, 8.6)	75	CH	3.13 (1H, dd, J = 7.8, 9.0)	75	CH	3.12 (1H, dd, J = 7.7, 7.9)
3′	77.9	CH	3.33 (1H, m)	77.9	CH	3.33 (1H, m)	77.9	CH	3.33 (1H, m)
4′	71.6	CH	3.29 (1H, m)	71.6	CH	3.29 (1H, m)	71.6	CH	3.24 (1H, m)
5′	78.1	CH	3.24 (1H, d, J = 4.5)	78	CH	3.25 (1H, d, J = 5.1)	78	CH	3.25 (1H, d, J = 5.0)
6′	62.8	CH_2	3.84 (1H, d, J = 11.2) 3.63 (1H, dd, J = 11.2, 4.5)	62.7	CH_2	3.83 (1H, d, J = 11.8) 3.63 (1H, dd, J = 11.8, 5.1)	62.7	CH_2	3.83 (1H, d, J = 11.8) 3.63 (1H, dd, J = 11.8, 5.0)

the protein and therefore the ligands must bind to AChE without inducing extensive alteration that includes unfolding or expansion. Also, the simulation allowed the R_g values to remain within a small range of 22.5 Å to 22.8 Å thus indicating the structural stability of the protein. These results indicate that the interaction between eserine or **WTH1** and AChE does not perturb its native conformation and that vesicles are required for the inhibitor activity of both compounds due to their effectiveness maintaining AChE architecture appropriate for proper ligand recognition. Further understanding of the dynamics between AChE and the inhibitors was obtained by further analysis of the solvent accessible surface area (SASA) as shown in Fig. 5G. The **WTH1** complex had an SASA of approximately 750 $Å^2$ indicating stable interaction within the complex. Surprisingly, eserine was as stable as **WTH1** with an average SASA of 730 $Å^2$. The fact that these ligands exhibit similar performance across both complexes suggests that they are good AChE inhibitors.

3.9. Binding free energy analysis

Therefore, stability of the system was assessed by tracking RMSD fluctuations as shown in Fig. 6. Binding free energy calculations were done from the 1–100 ns MD simulations using 10 000 randomly selected snapshots from 1. To assess the binding affinity of the selected compounds towards AChE, both MM/PBSA and MM/GBSA methods were used. Using the MM/PBSA method, the calculated binding free energies for the inhibitors **WTH1** (−43.54 kcal mol^{-1}) and Esorine (−42.70 kcal mol^{-1}) were obtained. The results in Table 6 indicate that **WTH1** possesses higher ΔG_{pred} (GB) values in AChE bound systems, suggesting higher affinity for the AChE active site. This is consistent with the fact that MM/GB/PB/SA values give better ΔG_{pred} values in comparison to those obtained from docking studies and confirms our methodology in assessing binding efficiency of putative AChE inhibitors. By decomposition of the total binding free energy to its individual components, the MM/GB/PBSA method allows for an increased understanding in the dynamics of the ligand–receptor interaction. Polar solvation energies of the complexes as shown in Fig. 6 are positive, partially cancelling the favorable electrostatic energies (ΔE_{ele}) in the gas phase for both complexes. Consequently, the formation of ligand–receptor complex is avoided as a result of unfavorable electrostatic contributions (ΔG_{ele} + $\Delta G_{ele,sol}$). However, negative values of van der Waals interactions and the nonpolar solvation energy (ΔE_{vdW} + $\Delta G_{nonpol,sol}$) contribute positively to the binding affinity of **WTH1** toward AChE. Notably, the ΔE_{vdW} values are larger than one does the ΔE_{ele} values in all systems, and in all systems the vdW and nonpolar interactions play an important role in improving the inhibitory effectiveness of AChE inhibitors.

Multiple hydrophobic amino acids such as W286, V294, W86, Y72, Y337, Y133, F297, F295, and F338 determine the level of binding efficiency. The interactions between **WTH1** inhibitors and AChE also depend significantly on electrostatic forces but show lower influence than van der Waals and nonpolar solvation effects. The electrostatic forces make eserine more effective in binding AChE than **WTH1**. The inhibitory potency of the AChE-**WTH1** (−51.5212 kcal mol^{-1}) as well as AChE-eserine (−37.4592 kcal mol^{-1}) complexes depends predominantly on van der Waals interactions according to their substantial negative ΔE_{vdW} results. The results demonstrate that van der Waals and hydrophobic forces play the most powerful role in determining the inhibitory properties of AChE inhibitors but electrostatic forces have a secondary influence. This study reveals critical information about binding interactions while showing that strengthening both van der Waals forces and hydrophobic bonding will lead to better AChE inhibitor design.

4. Conclusion

In this study, two new withanolide-type compounds, **WTH1** and **WTH2**, along with one known compound (**WTH3**), were successfully isolated and structurally characterized from the methanol extract of *Withania coagulans*. The methanol extract exhibited the highest total phenolic and flavonoid contents, correlating with potent antioxidant activity and significant inhibitory effects against key enzymes, including acetylcholinesterase (AChE), butyrylcholinesterase (BChE), lipoxygenase, α-glucosidase, and tyrosinase. Among the isolated compounds, **WTH1** demonstrated the strongest molecular interactions with AChE, favorable pharmacokinetic properties, high gastrointestinal absorption, chemical stability, and optimal binding free energy, as supported by molecular docking and Density Functional Theory (DFT) analyses. Overall, the successful isolation of two new bioactive withanolides (**WTH1** and **WTH2**), combined with their potent *in vitro* and *in silico* activities, underscores the therapeutic potential of *W. coagulans* as a natural source of agents for neurodegenerative, metabolic, inflammatory, and skin-related disorders. These findings provide a strong foundation for further pharmacological evaluation and development of these novel compounds.

Conflicts of interest

No potential conflict of interest was reported by the author(s).

Data availability

The data supporting this article have been included as part of the supplementary information (SI). Supplementary information is available. See DOI: https://doi.org/10.1039/d5ra04491j.

Acknowledgements

The author would like to thanks to University of Nizwa for general support of this work. The authors extend their appreciation to Taif University, Saudi Arabia for supporting this work through project number TU-DSPP-2024-19.

References

1 M. B. Bahadori, B. Asghari, L. Dinparast, G. Zengin, C. Sarikurkcu, M. Abbas-Mohammadi and S. Bahadori, *LWT*, 2017, **75**, 42–50.
2 D. M. Grochowski, S. Uysal, A. Aktumsek, S. Granica, G. Zengin, R. Ceylan, M. Locatelli and M. Tomczyk, *Phytochem. Lett.*, 2017, **20**, 365–372.
3 C. Jang, D. K. Yadav, L. Subedi, R. Venkatesan, A. Venkanna, S. Afzal, E. Lee, J. Yoo, E. Ji, S. Y. Kim and M.-h. Kim, *Sci. Rep.*, 2018, **8**, 14921.
4 A. Raza, T. A. Chohan, M. Sarfraz, T. A. Chohan, M. Imran Sajid, R. K. Tiwari, S. A. Ansari, H. M. Alkahtani, S. Yasmeen Ansari and U. Khurshid, *J. Biomol. Struct. Dyn.*, 2023, **41**, 14358–14371.
5 T. A. Chohan, H.-Y. Qian, Y.-L. Pan and J.-Z. Chen, *Mol. BioSyst.*, 2016, **12**, 145–161.
6 J. Cheung, M. J. Rudolph, F. Burshteyn, M. S. Cassidy, E. N. Gary, J. Love, M. C. Franklin and J. J. Height, *J. Med. Chem.*, 2012, **55**, 10282–10286.
7 A. Meden, D. Knez, M. Jukič, X. Brazzolotto, M. Gršič, A. Pišlar, A. Zahirović, J. Kos, F. Nachon, J. Svete, S. Gobec and U. Grošelj, *Chem Commun.*, 2019, **55**, 3765–3768.
8 X. Lai, H. J. Wichers, M. Soler-Lopez and B. W. Dijkstra, *Angew Chem. Int. Ed. Engl.*, 2017, **56**, 9812–9815.
9 N. C. Gilbert, S. G. Bartlett, M. T. Waight, D. B. Neau, W. E. Boeglin, A. R. Brash and M. E. Newcomer, *Science*, 2011, **331**, 217–219.
10 M. F. Khalid, K. Rehman, K. Irshad, T. A. Chohan and M. S. H. Akash, *Dose-Response*, 2022, **20**, 15593258221093275.
11 K. Rehman, T. A. Chohan, I. Waheed, Z. Gilani and M. S. H. Akash, *J. Cell. Biochem.*, 2019, **120**, 425–438.
12 A. Hamad, M. Abbas Khan, I. Ahmad, A. Imran, R. Khalil, T. Al-Adhami, K. Miraz Rahman, Quratulain, N. Zahra and Z. Shafiq, *Bioorg. Chem.*, 2020, **105**, 104336.
13 T. A. Chohan, T. A. Chohan, L. Zhou, Q. Yang, L. Min and H. Cao, *Toxins*, 2018, **10**, 425.
14 K. Rehman, S. M. Munawar, M. S. H. Akash, M. A. Buabeid, T. A. Chohan, M. Tariq, K. Jabeen and E.-S. A. Arafa, *PLoS One*, 2020, **15**, e0227637.
15 T. A. Chohan, H. Qian, Y. Pan and J.-Z. Chen, *Curr. Med. Chem.*, 2015, **22**, 237–263.
16 J. Iqbal, A.-u. Rehman, M. A. Abbasi, S. Z. Siddiqui, S. Rasool, M. Ashraf, A. Iqbal, S. Hamid, T. A. Chohan and H. Khalid, *Braz. J. Pharm. Sci.*, 2020, **56**, e18092.
17 T. A. Chohan, M. Sarfraz, K. Rehman, T. Muhammad, M. U. Ghori, K. M. Khan, I. Afzal, M. S. H. Akash, A. Malik and T. A. Chohan, *Saudi J. Biol. Sci.*, 2020, **27**, 3025–3034.
18 M. Younas, M. I. Rashid, K. Ashraf, M. Ijaz, M. Suleman, T. A. Chohan and S.-U. Rahman, Immunoinformatics-Assisted Design of Novel Multi-Epitope-Based Vaccine Against Rhipicephalus Microplus Tick, 2017, preprint, Available at SSRN 4414645.
19 H. Qian, J. Chen, Y. Pan and J. Chen, *Molecules*, 2016, **21**, 1222.
20 A. Arooj, M. T. Pervez, Z. Gillani, T. A. Chohan, M. Tayyab Chaudhry, M. E. Babar and A. T. Shah, *BioRxiv*, 2019, 602615.
21 S. A. Ejaz, A. Saeed, P. R. Birmani, K. M. Katubi, Z. M. Elqahtani, M. Al-Buriahi, R. Ujan, F. Siddique, S. b. Ahmed and Z. Alrowaili, *Plos one*, 2022, **17**, e0271602.
22 D. Case, T. Darden, T. E. Cheatham III, C. Simmerling, J. Wang, R. Duke, R. Luo, R. Walker, W. Zhang and K. Merz, *The Amber biomolecular simulation programs*, University of California, San Francisco, 2012, vol. 1.
23 H. Gohlke and D. A. Case, *J. Comput. Chem.*, 2004, **25**, 238–250.
24 D. Case, R. Betz, D. Cerutti, T. Cheatham, T. Darden and R. Duke, *Amber 16*, University of California, San Francisco, 2016.
25 T. A. Chohan, J.-J. Chen, H.-Y. Qian, Y.-L. Pan and J.-Z. Chen, *Mol. BioSyst.*, 2016, **12**, 1250–1268.
26 N. Kokila, B. Mahesh, R. Ramu, K. Mruthunjaya, B. Bettadaiah and H. Madhyastha, *J. Biomol. Struct. Dyn.*, 2023, **41**, 10642–10658.
27 Y. Yu, S. Xu, R. He and G. Liang, *J. Agric. Food Chem.*, 2023, **71**, 2684–2703.